

# **Congenital disorder of glycosylation caused by starting site-specific variant in syntaxin-5**

Peter T.A. Linders<sup>1</sup>, Eveline C.F. Gerretsen<sup>1</sup>, Angel Ashikov<sup>2,3</sup>, Mari-Anne Vals<sup>4,5</sup>, Rinse de Boer<sup>6</sup>, Natalia H. Revelo<sup>1</sup>, Richard Arts<sup>1</sup>, Melissa Baerenfaenger<sup>2</sup>, Fokje Zijlstra<sup>3</sup>, Karin Huijben<sup>3</sup>, Kimiyo Raymond<sup>7</sup>, Kai Muru<sup>5,8</sup>, Olga Fjodorova<sup>8</sup>, Sander Pajusalu<sup>5,8</sup>, Katrin Ōunap<sup>5,8</sup>, Martin ter Beest<sup>1</sup>, Dirk Lefeber<sup>2,3,\*</sup> and Geert van den Bogaart<sup>1,9,\*</sup>

<sup>1</sup> Department of Tumor Immunology, Radboud Institute for Molecular Life Sciences, Radboud University Medical Center, 6525 GA Nijmegen, The Netherlands

<sup>2</sup> Department of Neurology, Donders Institute for Brain, Cognition and Behavior, Radboud University Medical Center, 6525 GA, Nijmegen, The Netherlands

<sup>3</sup> Translational Metabolic Laboratory, Department of Laboratory Medicine, Radboud University Medical Center, 6525 GA, Nijmegen, The Netherlands

<sup>4</sup> Children's Clinic, Tartu University Hospital, Estonia

<sup>5</sup> Department of Clinical Genetics, Institute of Clinical Medicine, University of Tartu, Estonia

<sup>6</sup> Molecular Cell Biology, Groningen Biomolecular Sciences and Biotechnology Institute, University of Groningen, Groningen, The Netherlands

<sup>7</sup> Department of Laboratory Medicine and Pathology, Mayo College of Medicine, Rochester, Minnesota, USA.

<sup>8</sup> Department of Clinical Genetics, United Laboratories, Tartu University Hospital, Tartu, Estonia

<sup>9</sup> Department of Molecular Immunology, Groningen Biomolecular Sciences and Biotechnology Institute, University of Groningen, 9747AG, Groningen, Netherlands

\* Correspondence: [dirk.lefeber@radboudumc.nl](mailto:dirk.lefeber@radboudumc.nl); Tel.: +31-24-36-14567; [g.van.den.bogaart@rug.nl](mailto:g.van.den.bogaart@rug.nl); Tel.: +31-50-36-35230

## **Abstract**

The SNARE (soluble N-ethylmaleimide-sensitive factor attachment protein receptor) protein syntaxin-5 (Stx5) is essential for Golgi transport. In humans, the *STX5* mRNA encodes two protein isoforms, Stx5 Long (Stx5L) from the first starting methionine and Stx5 Short (Stx5S) from an alternative starting methionine at position 55. In

**NOTE: This preprint reports new research that has not been certified by peer review and should not be used to guide clinical practice.** this study, we identified a novel human disorder caused by a single missense substitution in the second starting

methionine (p.M55V), resulting in complete loss of the short isoform. Patients suffer from an early fatal multisystem disease, including severe liver disease, skeletal abnormalities and abnormal glycosylation. Primary human dermal fibroblasts isolated from these patients showed defective glycosylation, altered Golgi morphology as measured by electron microscopy and mislocalization of glycosyltransferases. Measurements of anterograde trafficking, based on biotin-synchronizable forms of Stx5 (the RUSH system), and of cognate binding SNAREs, based on Förster resonance energy transfer (FRET), revealed that the short isoform of Stx5 is essential for intra-Golgi transport. This is the first time a mutation in an alternative starting codon is linked to human disease, demonstrating that the site of translation initiation is an important new layer of regulating protein trafficking.

# **Keywords**

Syntaxin-5, ER-Golgi trafficking, glycosylation, secretory pathway, congenital disorders of glycosylation

## Introduction

In eukaryotes, proteins destined for the secretory pathway are synthesized at the endoplasmic reticulum (ER) and then transported to the Golgi apparatus, where they are sorted for their ultimate destinations at the *trans*-Golgi network. Central to this process is intracellular membrane fusion, which is mediated by members of the SNARE (soluble *N*-ethylmaleimide-sensitive factor attachment protein receptor) protein family. Cognate SNARE proteins that are present in both the carrier vesicle and target membranes, called v- and t-SNAREs respectively, engage and form a tight alpha-helical coiled-coil bundle that overcomes the energy barrier of membrane fusion. Membrane fusion requires a single R-SNARE, characterized by an arginine residue located central in the SNARE bundle, and three Q-SNAREs, with glutamine residues instead. Generally in mammalian cells, the R-SNAREs act as vesicle (v-) SNAREs and the Q-SNAREs together form the t-SNARE complex on the target membrane<sup>1</sup>. In contrast, the Qc-SNAREs Bet1 and Bet1L (GS15) function as the v-SNAREs at the ER/Golgi interface<sup>2-5</sup>, while, for anterograde ER to Golgi trafficking, the recipient t-SNARE complex is formed by the Qa-SNARE syntaxin-5 (Stx5)<sup>6-9</sup>, together with the Qb-SNAREs GosR1 (also known as GS27 or membrin) or GosR2 (GS28), and R-SNAREs Ykt6 or Sec22b (Ers24)<sup>10-12</sup>. This different allocation of the Qc-SNAREs Bet1 and Bet1L as v-SNARE instead of t-SNARE possibly prevents the formation of non-functional SNARE complexes during ER to Golgi transit. In addition, Stx5 functions in retrograde intra-Golgi transport by forming a recipient t-SNARE complex with GosR1, and Ykt6<sup>5,13</sup> and in retrograde trafficking from endosomes to the *trans*-Golgi network (TGN)<sup>14,15</sup>, making it a unique SNARE protein involved in both anterograde and retrograde Golgi transport.

STX5 is highly conserved and is an essential gene in animals and fungi<sup>16,17</sup>. In animals, Stx5 exists as a long and a short isoform translated from the same mRNA: 39.6 kDa sized Stx5 Long (Stx5L) and 34.1 kDa sized Stx5 Short (Stx5S)<sup>13,18</sup>. This is in contrast to lower organisms such as *Saccharomyces cerevisiae*, which only express a single isoform of Stx5 (Sed5p). Although Sed5p was originally believed to resemble mammalian Stx5S<sup>13</sup>, it is now clear that it likely more resembles Stx5L, since an N-terminal COPI-binding tribasic motif has been identified in Sed5p<sup>19</sup>. The emergence of a second Stx5 isoform can be traced back to the pacific purple sea urchin, *Strongylocentrotus purpuratus*, and is also present in the model organism *Danio rerio*, but not in *Drosophila melanogaster* nor *Caenorhabditis elegans*. Compared to Stx5S, Stx5L contains 54 extra N-terminal residues bearing an Arginine – Lysine – Arginine (RKR) ER retrieval motif, and as a result, Stx5L locates more to the ER whereas Stx5S locates more to the Golgi network<sup>13,18,20-22</sup>. The evolutionary necessity of the two Stx5 isoforms remains unclear but it has been suggested that Stx5L is important to maintain ER structure by binding

microtubules, possibly via CLIMP-63<sup>21,23</sup>. In addition, immunoprecipitations showed that GosR1 and Bet1L preferentially interact with Stx5S over Stx5L<sup>24,25</sup>, suggesting that Stx5S might act in more fusogenic complexes later at the ER-Golgi interface whereas Stx5L might be more involved in earlier fusion steps.

In the present study, we identified a genetic variant in the second translation codon methionine-55, fully abrogating the production of Stx5S and providing a unique opportunity to study the physiological relevance of the existence of two isoforms in humans. Patients homozygous for this mutation have a very severe clinical phenotype associated with infantile mortality and defective protein glycosylation. We demonstrate that although Stx5L can largely compensate for the lack of Stx5S, the loss of Stx5S leads to defects in intra-Golgi trafficking with mislocalization of glycosyltransferases, which results in pronounced defects in glycosylation. Moreover, by synchronizing the intracellular trafficking of Stx5 isoforms, we reveal differential trafficking routes for either isoform and identify Stx5S as the dominant Qa-SNARE for intra-Golgi transport. This is the first time that a mutation in an alternate starting site of ribosomal translation is related to human disease. This finding reveals that protein function can be regulated at the level of translation initiation and has profound effects on intracellular membrane trafficking and Golgi function.

## Results

### *Clinical data*

The family history (Supplementary Fig. 1) revealed multiple deceased individuals (IV:3, IV:9, IV:10) shortly after birth, spontaneous abortions (IV:5, IV:6, IV:7), and elective abortions in the 20th-21st week of pregnancy due to abnormal fetal ultrasound (US) (IV:4, IV:8). Fetal US of individuals IV:8, IV:9, and IV:10 (Fig. 1a-c, respectively) showed shortening of the long bones with suspicion of chondrodysplasia. Patients IV:9 and IV:10 showed highly dysmorphic facial features (high forehead, frontal bossing, prominent glabella, short and upturned nose, long philtrum, micrognathia and dysplastic ears), skeletal dysplasia (short extremities and narrow thorax), profound hypotonia, hepatomegaly, and many abnormal laboratory parameters including elevated cholesterol (Fig. 1b, c, Supplementary Table 1). After birth, the main clinical problem for both patients IV:9 and IV:10 was progressive liver failure with cholestasis and hyperinsulinemic hypoglycemia (Supplementary Table 1). Liver failure was the main cause of death at the age of between 0 and 3 month, and between 6 and 9 months, in patients IV:9 and IV:10, respectively. Autopsy of fetus IV:8 revealed bilateral hydronephrosis and sacral lordosis. Autopsy of patient IV:9 showed hepatomegaly with stage 3 to 4 liver fibrosis, agenesis of left kidney, hyperemia of internal

organs, ventricular septal defect and suggestive pathohistological features of chondrodysplasia. Autopsy of patient IV:10 showed biliary cirrhosis and nodular regenerative hyperplasia, pancreatic hypertrophy/hyperplasia, and narrow thorax with normal lung development.

#### ***Abnormal protein glycosylation suggests a defect in Golgi trafficking***

Known genetic causes for skeletal dysplasias were excluded (IV:8), no submicroscopic chromosomal abnormalities were found, while most metabolic investigations were normal except for the Congenital Disorders of Glycosylation (CDG) (IV:9 and IV:10). CDG screening revealed a strong hyposialylation of protein N-glycosylation and mucin-type O-glycosylation, as analyzed by isofocusing of respectively plasma transferrin (Fig. 1d, Supplementary Table 2) and apolipoprotein CIII (ApoCIII-IEF, Fig. 1e, Supplementary Table 2). ApoCIII-IEF showed a strong increase of non-sialylated apoCIII (ApoCIII-O) band intensities compared to the intensities of the fully glycosylated form, even stronger than observed for genetic defects in the Conserved Oligomeric Golgi (COG) complex, a known group of disorders with disturbed Golgi homeostasis and abnormal glycosylation<sup>26</sup>. To gain more insight into the abnormal N-glycan structures, mass spectrometry was performed of intact transferrin (Fig. 1f, g, Supplementary Fig. 2) and of total plasma protein derived N-glycans (Fig. 1f, h, Supplementary Fig. 3). Analysis of intact transferrin of individuals IV:9 and IV:10 revealed multiple abnormal glycan structures, divided into two categories: high mannose structures and truncated glycans. Compared to the peak height of completely glycosylated transferrin, a dominant accumulation was found of high-mannose glycans (Supplementary Table 3, Man5, mass/peak number) suggesting a problem with MGAT1, the enzyme that adds the next *N*-acetylglucosamine during N-glycosylation. Furthermore, a series of transferrin isoforms was observed with reduced incorporation of galactose and sialic acid residues. Similar glycosylation patterns were observed in COG5-CDG<sup>27–30</sup>. Analysis of N-glycans released from total plasma proteins recapitulated the two categories of abnormal glycans with the accumulation of high mannose glycans, as well as reduced incorporation of galactose and sialic acid residues (Supplementary Table 4). Together, these data indicate that the activities of multiple glycosyltransferases in the Golgi apparatus are affected, covering both N- and O-glycosylation, thereby suggesting a general disturbance in Golgi trafficking.

#### ***Molecular investigations result in the identification of variants in STX5***

Chromosomal microarray analysis (CMA) using HumanCytoSNP-12 microarrays revealed multiple long contiguous stretches of homozygosity (LCSH, >5 Mb) distributed across the entire genome, with several regions of homozygosity on chromosome 11 in all three affected sibs (IV:8, IV:9 and IV:10, **Supplementary Table 5**). Exome sequencing was performed in proband IV:9 to find the genetic variant that could be associated with the disease. Only two homozygous rare protein-altering variants without homozygous individuals in the gnomAD v3 database were identified in shared homozygous stretches on chromosome 11. First, a missense variant in the *VPS37C* gene was discovered (NM\_017966.4:c.760G>T p.(Gly254Cys) rs201088253). However, as this variant reaches an allele frequency of 0.9% in Estonia, it is unlikely to cause a rare genetic disorder. The second variant was identified in the *STX5* gene (NM\_003164.4:c.163A>G p.(Met55Val), **Fig 2a**). This is a missense mutation affecting the alternative starting codon for the production of the short Stx5 isoform. The variant is absent from the gnomAD v3 database and was thus classified as a potentially disease-causing variant. The variant was confirmed by Sanger sequencing as homozygous in all affected individuals (IV:8, IV:9, and IV:10) and as heterozygous in the mother (III:2). Paternal DNA was not available for testing.

To confirm the effect of the genetic variant on both Stx5 proteoforms, immunoblotting was performed in primary dermal fibroblasts of patients IV:9 and IV:10. While Stx5L was present, a total absence of Stx5S was found in both patient fibroblasts (**Fig. 2b, c**). We next tested the expression of known interaction partners of Stx5. The levels of Qc-SNARE Bet1L, which forms a complex with Stx5 upon retrograde intra-Golgi trafficking<sup>5,13-15</sup>, were also reduced. In contrast (**Fig. 2b, c**), the expression of Qc-SNARE Bet1, which forms a complex with Stx5 upon anterograde ER-Golgi trafficking<sup>10,12,13,31</sup> was not reduced (**Fig. 2b, c**). Likewise, the expression of Qb-SNAREs GosR1 and GosR2, which can complex with Stx5 for anterograde ER-Golgi trafficking and retrograde intra-Golgi trafficking<sup>5,9,10,12,13,24</sup> were unaltered in patient dermal fibroblast lysates. We hypothesized that a compensatory mechanism might exist by upregulating the expression of the *trans*-Golgi Qa-SNARE Stx16<sup>32</sup>, usually involved in endosome-to-TGN trafficking<sup>33</sup>, but we did not detect a change of Stx16 expression in patient fibroblast lysates (**Fig. 2b, c**). As a first step to confirm that fibroblasts offer a useful model to recapitulate the cell biological abnormalities due to loss of the Stx5S isoform, we studied glycosylation by fluorescently-labeled lectins.

#### ***Glycosylation defects in Stx5M55V patient fibroblasts***

Patient fibroblasts could be cultured normally and we did not observe apparent differences in growth rate or viability between healthy control and patient-derived cell lines. Cell surface staining with the lectin SNA-I from *Sambucus nigra*, which binds terminal sialic acid in an  $\alpha$ -2,6 linkage of fully-formed N-glycan moieties and, to a lesser extent, sialic acid in an  $\alpha$ -2,3 linkage, showed that glycosylation was also impaired at the cellular level in patient fibroblasts. Compared to fibroblasts of healthy donors, we observed a more than two-fold reduced SNA-I labeling intensity in Stx5M55V patient fibroblasts (Fig. 2d,e). Moreover, most signal came from punctuated structures in the Stx5M55V patient fibroblasts, instead of the more uniform cell membrane labeling observed in the healthy donor fibroblasts. To confirm this glycosylation defect, we performed cell surface staining with the lectin PNA (Peanut agglutinin) from *Arachis hypogaea*, which binds terminal galactose residues present on mucin O-glycan moieties of incompletely glycosylated proteins. Opposite to our findings with SNA-I, we observed an increased labeling intensity in Stx5M55V patient fibroblasts relative to healthy control by about six-fold (Fig. 2f,g). These findings show that patient-derived fibroblasts, which express Stx5L but lack Stx5S, have a glycosylation defect.

Next, we evaluated the expression levels of Stx5S and Stx5L in lysates of peripheral blood mononuclear cells (PBMCs) obtained from four different healthy donors (Supplementary Fig. 4). While total Stx5 expression levels varied strongly (more than two-fold), the ratio of Stx5S and Stx5L was approximately equimolar for all individuals, demonstrating that the expression ratio is similar in PBMCs of different healthy subjects.

To determine the role of Stx5S in Golgi transport, we generated a Stx5L-lacking fibroblast cell line from one of the prior used control lines, using CRISPR/Cas9 (Fib Stx5 $\Delta$ L, Supplementary Fig. 5a). We then performed the same cell surface staining as described above. While we observed a similar decrease in SNA-I labeling intensity in Stx5 $\Delta$ L fibroblasts as in Stx5M55V patient fibroblasts, the staining pattern was more similar to healthy control and showed a uniform plasma membrane-localized SNA-I labeling (Supplementary Fig. 5b-c). In addition, opposite to Stx5M55V fibroblasts, the low PNA labeling intensity was reduced further in Fib Stx5 $\Delta$ L (Supplementary Fig. 5d-e). To investigate this difference further, we generated two clonal HeLa cell lines lacking Stx5L using the same method (Stx5 $\Delta$ L: B1A7 and C1F4, Supplementary Fig. 5f), and we observed a decrease in the already low SNA-I labeling intensity as measured by FACS compared to the parental HeLa cells, while PNA labeling resulted in opposite changes between the two Stx5 $\Delta$ L lines (Supplementary Fig. 5g-k). The difference in PNA labeling between the HeLa Stx5 $\Delta$ L cell lines therefore likely is attributable by clonal variation and/or off-

target effects of CRISPR/Cas9. These results demonstrate that while the loss of Stx5S or Stx5L both result in N-glycosylation defects, the defect is stronger upon the loss of Stx5S, as this results in lower levels and a punctuated distribution of sialic acid moieties. Moreover, the mucin-type O-glycosylation defect seems specific to the loss of Stx5S. As these results reiterate the glycosylation defect observed on serum transferrin, total plasma N-glycans and apoCIII mucin O-glycans, patient fibroblasts are a suitable model to investigate the cell biological consequences of the complete disruption of the Stx5S isoform.

### ***Stx5M55V mutation results in mislocalization of glycosyltransferases***

Given that Stx5 mediates ER-Golgi trafficking<sup>5,7,9–13,15,24,31</sup>, we next investigated whether the glycosylation defect in Stx5M55V patient fibroblasts was caused by the mislocalization of glycosyltransferases. We performed immunofluorescence labeling of mannosyl ( $\alpha$ -1,3)-glycoprotein  $\beta$ -1,2-N-acetylglucosaminyltransferase (MGAT1, also known as GnTI), which catalyzes the addition of GlcNAc to the immature man-5 N-glycan. Compared to healthy donor fibroblasts, MGAT1 colocalizes only slightly less with the *cis*-Golgi marker GM130 in patient fibroblasts (Fig. 3a, b), but colocalized substantially less with the *trans*-Golgi network marker TGN46 (Fig. 3c, d). In addition, alpha-mannosidase 2 (MAN2A1), which catalyzes the final hydrolytic step in the N-glycan maturation pathway after MGAT1 conversion, colocalized substantially less with both GM130 (Supplementary Fig. 6a, b) and TGN46 in patient fibroblasts (Supplementary Fig. 6c, d). Similarly to MGAT1, beta-galactoside alpha-2,6-sialyltransferase 1 (ST6GAL1), which catalyzes the transfer of sialic acid to galactose residues of N-glycans in an  $\alpha$ -2,6 linkage, colocalized less with both GM130 (Supplementary Fig. 6e, f) and TGN46 in patient fibroblasts (Supplementary Fig. 6g, h). Finally, N-acetylgalactosaminyltransferase 2 (GALNT2), which catalyzes the initial reaction in mucin O-linked glycan synthesis, localized more to the *cis*-Golgi (marker Zinc finger protein-like 1 (ZFPL1)<sup>35</sup>) (Fig. 3e, f) and less to the *trans*-Golgi in patient fibroblasts (Fig. 3g, h).

To exclude the possibility that our conclusions were affected by potential mislocalization of TGN46 in the patient cells, we repeated these experiments but now co-stained for another *trans*-Golgi marker, the *trans*-Golgi coiled-coil protein p230<sup>36</sup> (Supplementary Fig. 7). Indeed, we observed similar Pearson correlation coefficients for p230 as for TGN46 with MGAT1, GALNT2, MAN2A1, and ST6GAL1 (Supplementary Fig. 7). Moreover, to confirm that the observed changes in colocalization were not due to lower expression of glycosyltransferases, we performed immunoblotting for several glycosyltransferases and could not detect consistent differences between control and Stx5M55V fibroblasts, although we noticed substantial variation in protein expression levels of some of the



glycosyltransferases between the samples (Supplementary Fig. 8), reflecting expression differences among individuals and/or fibroblast lines.

Taken together, the loss of Stx5S results in irregular localization of glycosyltransferases to the Golgi apparatus. An altered Golgi organization and mislocalization of glycosyltransferases can have a profound impact on glycosylation as shown by computational simulations<sup>37</sup>. We investigated the organization of the Golgi complex in Stx5M55V fibroblasts in more detail.

### ***Stx5S mediates retrograde Golgi-ER and intra-Golgi trafficking***

Transmission electron microscopy showed dilation of rough ER and Golgi cisternae in the Stx5M55V patient fibroblasts (Fig. 4a-c, gallery Supplementary Fig. 9), similar to previously observed alteration in the ultrastructure of the Golgi in several COG defects<sup>38–40</sup>. Notwithstanding these large alterations in Golgi morphology, the polarized arrangement of Golgi apparatus cisternae was still present in Stx5M55V, as observed by immunofluorescence labeling of *cis*- and *trans*-Golgi markers (Supplementary Fig. 10). These results indicate that although Stx5L is sufficient to maintain normal Golgi apparatus cisterna polarization, Stx5S is required for physiological ER and Golgi ultrastructure and proper trafficking of glycosylation enzymes.

To address the role of the Stx5 isoforms in more detail, we studied the distribution of Stx5 isoforms in the Golgi network. Because Stx5L contains an RKR ER-retrieval motif in its N-terminal extension, it locates more at the ER compared to Stx5S<sup>13,18,20,21</sup>. In line with this, we observed a more dominant localization of Stx5L at the ER and less at various Golgi compartments in Stx5M55V fibroblasts compared to total Stx5 localization in healthy control fibroblasts (Supplementary Fig. 11a, b, d, e, Supplementary Fig. 12a, b, d, e).

A notable difference was the far more diffuse staining in Stx5M55V patients of the COPI coat protein  $\beta$ COP (Supplementary Fig. 11a, c) and of TGN46 (Supplementary Fig. 11d, f). In contrast, we observed a small increase in GM130 fluorescence in Stx5M55V patients (Supplementary Fig. 12f). Since Western blot showed that total cellular levels of  $\beta$ COP and GM130 were not consistently altered in Stx5M55V patients (Supplementary Fig. 11g), the more diffuse staining of  $\beta$ COP is suggestive of reduced association with COPI-coated vesicles, while the higher staining intensity of GM130 suggests more association with the *cis*-Golgi. In contrast, total TGN46 protein levels were somewhat reduced in patient fibroblasts (Supplementary Fig. 11h). These findings suggest that loss of Stx5S results in reduced COPI trafficking between GM130-marked *cis*- and TGN46-marked *trans*-Golgi compartments.

Using an antibody specific to Stx5L (antibody specificity validated in [Supplementary Fig. 13](#)), we next investigated whether the loss of Stx5S affects the intracellular distribution of Stx5L. An altered cellular localization of Stx5L might imply a compensatory mechanism. Indeed, in Stx5M55V, Stx5L localizes more to the *cis*-Golgi as measured by increased colocalization with GM130 ([Fig. 4d, e](#)). A slight increase in ER localization as measured by PDI colocalization was also observed ([Fig. 4f, g](#)). Taken together, the loss of Stx5S causes Stx5L to relocate more towards the *cis*-Golgi.

As COPI is involved in retrograde Golgi-ER transport<sup>41</sup>, we investigated whether trafficking at this interface is compromised in Stx5M55V fibroblasts by using the fungal metabolite Brefeldin A (BFA), which inhibits COPI vesicle formation<sup>42</sup>. If loss of Stx5S results in reduced retrograde Golgi-ER transport, we expect reduced relocalization of Golgi-resident proteins to ER upon BFA treatment. Indeed, redistribution of GALNT2 from the Golgi to the ER was incomplete in patient fibroblasts ([Fig. 5a-c](#)), supporting a role for Stx5S in retrograde COPI trafficking. In addition, washout of BFA caused a more rapid localization of GALNT2 to the Golgi apparatus in Stx5M55V, likely due to its incomplete redistribution to the ER ([Fig. 5a, b, d, Supplementary Fig. 14a-c](#)). We investigated the role of Stx5L in Golgi trafficking further using temperature-synchronizable vesicular stomatitis virus G protein (VSVG) fused to GFP<sup>43</sup> in patient fibroblasts. At 40°C, VSVG does not fold correctly and the VSVG-GFP protein remains trapped in the ER. A temperature shift to 32°C enables the correct refolding of VSVG resulting in the synchronized release of VSVG-GFP from the ER, transit through the Golgi network, and finally delivery at the plasma membrane where it becomes accessible to antibody labeling. VSVG-EGFP appears at a Golgi-like compartment in both control and Stx5M55V fibroblasts at 30 mins after temperature shift from 40°C to 32°C ([Supplementary Fig. 14d](#)), but after 60 mins plasma membrane localization of VSVG is strongly reduced in Stx5M55V fibroblasts ([Fig. 5e-g](#)). Taken together, these findings show that Stx5L is sufficient for anterograde trafficking until the Golgi, but the loss of Stx5S significantly impairs intra- and/or post-Golgi trafficking, likely by the decrease of Stx5S-mediated intra-Golgi trafficking.

To further delineate the role of Stx5L in retrograde Golgi-ER trafficking, we performed a BFA experiment in the Stx5L-lacking HeLa cells. In these cells, BFA resulted in faster relocalization of GALNT2 to the ER compared to parental HeLa ([Supplementary Fig. 15a, b](#)), indicating that Stx5S suffices for retrograde COPI trafficking and the expression of Stx5L counteracts this process. Further investigation of anterograde ER-Golgi trafficking in Stx5ΔL cells with H-89 washout ([Supplementary Fig. 15c, d](#)), the retention using selective hooks (RUSH) system for synchronized ER-Golgi transport<sup>44</sup> ([Supplementary Fig. 15e, f, Supplementary Movies 1, 2](#)) and temperature-

synchronizable VSVG<sup>43</sup> (Supplementary Fig. 15g, h, Supplementary Movies 3, 4) revealed no phenotype relating to the loss of Stx5L. Thus, these data suggest Stx5L has no necessary function in ER-Golgi trafficking as Stx5S can compensate, while Stx5L can only partly compensate for the loss of Stx5S in retrograde Golgi-ER and intra-Golgi transport.

### ***Faster Golgi exit of Stx5L due to ER-retrieval motif***

Our results in patient fibroblasts indicate differential trafficking roles of the two Stx5 isoforms in ER-Golgi trafficking. To gain more insight in this process, we fused each Stx5 isoform to streptavidin-binding protein (SBP) and mCitrine (Stx5L-SBP-mCitrine and Stx5S-SBP-mCitrine; Stx5L-SBP-mCitrine carries the M55V mutation to suppress expression of Stx5S). Moreover, we generated a mutant form of Stx5L where the RKR ER-retrieval motif was converted to 3x alanine (AAA) (Stx5L $\Delta$ ER-SBP-mCitrine)<sup>18</sup>, to delineate the role of this motif in ER-Golgi transport. The co-expression of these constructs with ER-localized streptavidin enabled the synchronized release of the Stx5 fusion proteins from the ER using biotin, which is the so-called RUSH system<sup>44</sup> (Fig. 6a). Co-expressing each Stx5 isoform with the Golgi marker Giantin fused to mScarlet<sup>45</sup> in HeLa cells, allowed to visualize the trafficking of Stx5-SBP-mCitrine to the Golgi following the addition of biotin (Fig. 6a, b, Supplementary Movies 5-7). All three constructs were expressed at similar levels, as judged from the fluorescent intensities, and all Stx5 forms reached the Golgi with the same rate and achieved maximal Golgi localization after about 20 minutes (Fig. 6c). However, the subsequent decrease in Golgi localization, attributed to recycling to the ER or degradation of the fusion proteins, was faster for Stx5L-SBP-mCitrine than for Stx5S or Stx5L $\Delta$ ER (Fig. 6c, d). Thus, the RKR ER retrieval motif of Stx5L is necessary and sufficient for the attenuated presence of Stx5L at the Golgi, supporting that the main role of Stx5S is COPI trafficking specifically at the Golgi.

### ***The two isoforms of Stx5 differently engage in SNARE complexes***

Since interactions of Stx5 with Bet1 and Bet1L mediate anterograde ER-Golgi transport and retrograde intra-Golgi transport, respectively<sup>2-5</sup>, we hypothesized that Stx5S would interact more strongly with Bet1L, whereas Stx5L would interact more strongly with Bet1. We set out to test this hypothesis by performing co-immunoprecipitation with our RUSH Stx5 constructs. However, we were unable to consistently resolve differences in binding to endogenous cognate Qc-SNAREs between the two Stx5 isoforms, either with or without 30 mins biotin (Supplementary Fig. 16). A likely explanation is that interactions might occur *in vitro* during the

immunoprecipitation. Therefore, we developed an approach to visualize SNARE complexes based on a combination of the RUSH system<sup>44</sup> and our previously developed Förster resonance energy transfer-fluorescence lifetime imaging microscopy (FRET-FLIM) approach for visualization of SNARE complexes<sup>46</sup> (Fig. 7a). This FRET-FLIM approach employed Stx5 isoforms C-terminally fused with a donor fluorophore (mCitrine) and Bet1L C-terminally fused with an acceptor fluorophore (mCherry). The formation of a post-fusion SNARE complex results in the close proximity of the donor and an acceptor fluorophore resulting in FRET which can be measured from a decreased donor fluorescence lifetime ( $\tau$ ). Contrary to ratiometric FRET, FRET-FLIM is not dependent on local concentration differences or excitation intensities of the donor and acceptor fluorophores, as  $\tau$  is an intrinsic property of the fluorophore itself. By combining the FRET-FLIM approach with the RUSH system, we were able to control the spatial localization of Stx5 isoforms and measure interactions specifically at the ER (no biotin) or the Golgi apparatus (20 min after biotin addition). 30 minutes prior to imaging, cells were incubated with cycloheximide in culture medium to make sure background interaction from any ER-localized newly-synthesized acceptor construct was mitigated.

For the mCitrine donor-only Stx5 constructs, we measured similar lifetimes for both isoforms (Fig. 7c, Supplementary Fig. 17a, Stx5L: 3.02 ns  $\pm$  0.004, Stx5S: 2.99 ns  $\pm$  0.007) prior to biotin addition, while these lifetimes slightly decreased following biotin addition (Fig. 7d, Supplementary Fig. 17a, Stx5L: 2.90 ns  $\pm$  0.006, Stx5S: 2.86 ns  $\pm$  0.011). We attribute this reduced lifetime to the fact that mCitrine is somewhat pH-sensitive<sup>47</sup> and the pH of the Golgi apparatus is lower than in the ER lumen<sup>48</sup>. We then co-expressed the Stx5 isoforms with mCherry-tagged Bet1L (Bet1L-mCherry) (Fig. 7a,b). At the ER, thus before the release of Stx5 with biotin, we observed reduced lifetimes for both Stx5S and Stx5L with Bet1L-mCherry, compared to the donor-only controls (Fig. 7b, c, Stx5L: 2.82 ns  $\pm$  0.01, Stx5S: 2.79  $\pm$  0.01), whereas the lifetimes of Stx5S and Stx5L did not significantly differ from each other. After the release in the presence of biotin, this difference between Stx5L and Stx5S became significant and lifetimes were 2.63 ns ( $\pm$  0.01) for Stx5L while Stx5S dropped to 2.52 ns ( $\pm$  0.03) (Fig. 7b, d). To validate that the observed effect is indeed caused by functional SNARE complex formation, we repeated this experiment with VAMP8 instead of Bet1L as the acceptor R-SNARE. VAMP8 has no role in ER-Golgi membrane fusion but rather associates with the late endosomal/lysosomal compartment<sup>33,46,49–53</sup>. We only observed minor decreases in fluorescence lifetimes for both Stx5L and Stx5S (Supplementary Fig. 17b, c, prior to biotin Stx5L: 2.92 ns  $\pm$  0.01, Stx5S: 2.86  $\pm$  0.02, upon biotin addition Supplementary Fig. 17b, d, Stx5L: 2.82 ns

$\pm 0.01$ , Stx5S:  $2.76 \pm 0.02$ ). These FLIM results demonstrate that Stx5S interacts more strongly with Bet1L at the Golgi than Stx5L. Thus, Stx5S is the dominant Qa-SNARE for intra-Golgi trafficking.

## Discussion

Since the advent of the genomic age, close to 6,000 monogenic disorders have been discovered<sup>54</sup>. While nearly all of these disorders result in a truncated, unstable and/or nonfunctional protein, e.g., due to a genetic variant in the catalytic site or protein misfolding, isoform-specific mutations are rare. Here we present the first known mutation in an alternate site of ribosomal translation leading to human disease, namely the mutation of the second starting methionine of Stx5. This mutation leads to the complete and specific loss of Stx5S. Although *STX5* is an essential gene for embryonic development in mice<sup>16,17</sup>, here we show that in humans the loss of Stx5S still allowed a completed pregnancy. Nevertheless, patients have a very severe clinical pathology characterized by infantile mortality due to liver disease, skeletal abnormalities and protein glycosylation defects. While the exact mechanism for alternative translation is unclear, this might be an actively regulated process. It could also be simply regulated by the affinity of the ribosome for the nucleotide sequence upstream of the starting codon. Supporting the latter option, analysis of translation initiation sites with NetStart<sup>55</sup> revealed that the starting codon of Stx5S is located in a more optimal nucleotide context than the starting codon for Stx5L (Supplementary Fig. 18). This could lead to more leaky ribosomal scanning<sup>56,57</sup>, resulting in the more or less equimolar ratio of expression of Stx5L and Stx5S that we observed in fibroblasts and PBMCs of healthy individuals. On the other hand, Western blot revealed different ratios of the two Stx5 isoforms in different organs in rats<sup>18</sup>, suggesting (i) that different cell types express different levels of Stx5S and Stx5L and this is probably related to their exocytic function, and (ii) that the initiation of starting translation might be regulated and not merely dependent on the binding affinities of the ribosome.

Cofractionation and microscopy studies have revealed that the localization of Stx5L and Stx5S overlap to a large extent, but that they are generally distributed as a gradient between ER, ERGIC, and Golgi apparatus<sup>20</sup>. This observation has previously led to the suggestion that Stx5L might play a role in early Golgi trafficking, while Stx5S functions in late Golgi trafficking<sup>5,7,9-13,15,24,31</sup>. Our data now shows that this is not the case and that both Stx5 isoforms can mediate both early and late anterograde and retrograde Golgi trafficking with sufficient fidelity to keep the layered Golgi morphology intact. However, the role of Stx5S is more important for retrograde Golgi-ER and intra-Golgi trafficking, and its absence leads to an altered ER and Golgi morphology, distribution of

glycosylation enzymes and trafficking proteins. The cumulative effect of slight mislocalization of all glycosyltransferases might well explain the observed hypoglycosylation in the Stx5M55V patients. Indeed, recent modeling showed that the slight mislocalization of glycosyltransferases can result in large differences in glycosylation patterns, because glycosylation is the result of the sequential addition and removal of different sugar moieties at the various Golgi compartments<sup>37</sup>.

The dominant role of Stx5S in retrograde Golgi-ER and intra-Golgi trafficking is corroborated by the observation that cellular levels of Bet1L, with known roles in intra-Golgi trafficking, are lower in Stx5M55V patient cells. Interestingly, genetic variants in conserved oligomeric Golgi (COG) tethering complex components, which are also implicated in CDGs, also resulted in lower levels of Bet1L as well and this was attributed to a mislocalization of Bet1L to the ER where it was degraded<sup>58</sup>. Possibly, a similar mechanism might explain the reduction in Bet1L levels in Stx5M55V patients. Although the Stx5-Bet1L interaction has been reported in several studies<sup>14,41</sup>, our study now shows this interaction *in situ* using FLIM. This interaction is localization dependent and occurs mostly when Stx5 is localized at the Golgi. Moreover, we observed stronger interaction of Bet1L with Stx5S compared to Stx5L at the Golgi, which is likely the result of the differential localization of both isoforms.

An important function of the Golgi apparatus is protein glycosylation<sup>59</sup>. Collectively, somatic mutations affecting glycosylation are classified as CDGs and currently over 100 monogenic diseases affecting glycosylation have been identified<sup>60,61</sup>. A significant number of these include defects in Golgi trafficking, such as the components of the conserved oligomeric Golgi tethering complex (COG)<sup>38,62–69</sup>, mutations in genes coding for the vacuolar H<sup>+</sup>-ATPase and its assembly factors<sup>70–73</sup>, and novel genes involved in Golgi ion homeostasis<sup>74–76</sup>. Furthermore, defects are known in components associated with COPI-coated vesicles<sup>77</sup> that result in deficient protein glycosylation in patient cells, but are not linked to abnormal glycosylation of proteins in plasma and thus escape routine CDG screening. Our study is the first example of an ER-Golgi SNARE being implicated in CDG, thus highlighting the potential of glycosylation screening in patients to uncover novel cell biological mechanisms.

While the cellular effects of the loss of Stx5S in Stx5M55V mutant fibroblasts are subtle, there can be pronounced consequences in secretory cells, such as exocrine and endocrine cells, which are sensitive to minor disruptions of the secretory pathway<sup>59,77–79</sup>. Not only can the defects in intra-Golgi trafficking explain the hypoglycosylation in Stx5M55V patients, but also of other pathologies. For instance, Stx5 can participate in the trafficking and processing of the very low-density lipoprotein receptor (VLDL-R) and this role is heavily

dependent on the expression of Stx5<sup>80</sup>, thus providing an explanation for the observed cholesterol homeostasis defect with elevated cholesterol in all Stx5M55V patients.

In summary, we have demonstrated that a mutation in an alternative translation start site in Stx5 has a severe impact on intracellular membrane trafficking, leading to the discovery of a novel CDG. While there are many previous descriptions of alternative start site variations leading to disease<sup>81</sup>, this is the first known mutation in an alternative starting codon leading to human disease by the loss of an isoform.

## Acknowledgments

We thank the family for participating in this study. We thank the following people for constructs: Hesso Farhan and Franck Perez (Str-KDEL\_ManII-SBP-EGFP; Addgene plasmid #65252), Jennifer Lippincott-Schwartz (pEGFP-VSVG; Addgene plasmid #11912), Feng Zhang (pSpCas9n(BB)-2A-Puro (PX462) V2.0; Addgene plasmid #62987) and Dorus Gadella (pmScarlet-i\_Giantin\_C1, Addgene plasmid #85050). We also thank the Microscopic Imaging Center of the Radboud Institute for Molecular Life Sciences for use of their microscopy facilities. N.H.R. is funded by a Long-Term Fellowship from the European Molecular Biology Organization (EMBO-LTF, ALTF 232-2016) and a Veni grant from the Netherlands Organization for Scientific Research (016.VENI.171.097). G.v.d.B. is funded by a Young Investigator Grant from the Human Frontier Science Program (HFSP; RGY0080/2018) and a Vidi grant from the Netherlands Organisation for Scientific Research (NWO-ALW VIDI 864.14.001). G.v.d.B. has also received funding from the European Research Council (ERC) under the European Union's Horizon 2020 research and innovation program (grant agreement No. 862137). D.J.L. is funded by a Vidi grant (ZONMW VIDI 917.13.359), a ZONMW Medium Investment Grant (40-00506-98-9001) from the Netherlands Organisation for Scientific Research, and Erare grants EUROCDG2 and Euroglycanomics. K.Õ, M.-A.V., S.P., and K.M. were supported by the Estonian Research Council grants GARLA8175, PUT355, PUTJD827 and PRG471.

## Author Contributions

P.T.A.L., M.t.B., D.J.L., and G.v.d.B. designed the experiments and wrote the paper. E.C.F.G. contributed to the Stx5 kinetics, co-immunoprecipitation, and FLIM experiments. A.A., M.-A.V., M.B., F.Z., K.H., K.R., K.M., and K.Õ. contributed to the clinical data, exome sequencing and glycomics. O.F. and S.P. performed homozygosity mapping and prioritization of exome variants. N.H.R. and R.d.B. performed TEM. R.A. contributed to the Stx5ΔL



experiments. P.T.A.L. and M.t.B. performed all other experiments. All authors contributed to writing the manuscript.

## Declaration of Interests

The authors declare that they have no competing financial interests.

## Methods

### *Ethics*

The study was approved by Research Ethics Committee of the University of Tartu (approval dates 19.12.2011, 20.02.2012 and 17.03.2014, and approval numbers 210/M-17, 212/M-31 and 235/M-13, 17.03.2014, respectively) and were strictly in accordance with the Declaration of Helsinki. Informed consent for carrying out research was obtained from the family of investigated individuals. Buffy coats and whole blood were obtained as anonymous coded specimens from the Dutch blood bank (Sanquin) and were handled according to known practice and legal guidelines. The research with human blood samples at the Department of Tumor Immunology complies with all institutional and national ethics regulations and has been approved by the ethics committee of Sanquin.

### *Glycosylation studies*

Screening for CDG was carried out as described before<sup>71</sup>. Plasma N-glycan profiling was performed by MALDI-TOF mass spectrometry of permethylated glycans<sup>82</sup>, using 10 µL of plasma. High resolution mass spectrometry of intact transferrin was performed on a 6540 nanochip QTOF (Agilent), according to published protocols<sup>83</sup>.

### *Microarray analysis*

DNA was extracted either from peripheral blood according to the standard salting out protocol (IV:9 and IV:10) or from amniotic fluid cell culture (IV:8). Screening for chromosomal abnormalities was performed using HumanCytoSNP-12 BeadChips (Illumina Inc., San Diego, CA, USA). 200 ng of total DNA per sample was processed according to the protocol supplied by the manufacturer. Genotypes were called by GenomeStudio v2011.1 software and the data were analyzed using GenomeStudio Genome Viewer tool (Illumina Inc.). The minimum threshold for LCSH (long contiguous stretches of homozygosity) regions was set at 5 Mb.



# *Exome sequencing*

Genomic DNA was extracted from fibroblasts from patient IV:9 according to the manufacturer's protocol using a Qiagen Mini Kit (Qiagen) and was checked for DNA degradation on agarose gels. Next generation sequencing (NGS) and analysis were performed as described<sup>72</sup>. In brief, exome enrichment was performed using the SureSelect Human All Exon 50 Mb Kit (Agilent), covering ~21,000 genes. The exome library was sequenced on a SOLiD 5500xl sequencer (Life Technologies). Color space reads were iteratively mapped to the hg19 reference genome with the SOLiD LifeScope software version 2.1. Called variants and indels were annotated using an in-house annotation pipeline<sup>84,85</sup> and common variants were filtered out based on a frequency of >0.5% in dbSNP and a frequency of >0.3 % in our in-house database of >5,000 exomes. Quality criteria were applied to filter out variants with less than 5 variant reads and less than 20% variation. Furthermore, synonymous variants, deep intronic, intergenic and UTR variants were excluded. The identified variant was confirmed by Sanger sequencing in all affected individuals (IV:8, IV:9, and IV:10) and their mother (III:2). Paternal DNA (III:1) was not available.

# *Cell culture*

HeLa cells (authenticated by ATCC through their human STR profiling cell authentication service), including Stx5ΔL cell lines, were maintained in high glucose DMEM with Glutamax (Gibco 31966021). Human primary dermal fibroblasts were obtained from patients or healthy donors and maintained in Medium 199 with EBSS and L-glutamine (Lonza BE12-119F). All media were supplemented with 10% fetal calf serum (FCS, Greiner Bio-one, Kremsmünster, Austria) and antibiotic-antimycotic solution (Gibco 15240-062). All cells were regularly tested for mycoplasma contamination. Human peripheral blood mononuclear cells (PBMCs) were obtained from buffy coats as previously described<sup>86</sup>.

# *Plasmids and transfection*

Str-KDEL\_ManII-SBP-EGFP was a gift from Franck Perez (Addgene plasmid #65252). VAMP8-mCherry was constructed earlier<sup>46</sup> and previously deposited to Addgene (Addgene plasmid #92424). Str-KDEL\_Stx5L-SBP-mCitrine and Str-KDEL\_Stx5S-SBP-mCitrine were constructed by replacing the ManII-SBP-EGFP cassette in Str-KDEL\_ManII-SBP-EGFP using the AscI and XbaI restriction sites. Stx5 coding sequences were codon-optimized for *Homo sapiens* using JCat and ordered from Genscript, the Stx5L coding sequence carries the M55V mutation

to suppress production of Stx5S. Stx5LΔER coding sequence was generated with Q5-polymerase site-directed mutagenesis, using the Stx5L cDNA as a template with the following primer: 5'- CTTCG AATTC AATGA TTCCG GCCGC CGCCT ACGGC AGCAA GAACA CC. Sequences were verified with Sanger sequencing. HeLa cells were transfected with plasmid vectors using Fugene HD (Promega E2311), using the recommended protocol of the manufacturer. Only cells expressing low to moderate levels of the transfected plasmids, based on fluorescence intensity and manual localization scoring, were chosen for subsequent microscopic analyses.

#### *CRISPR/Cas9*

Stable knock out of Stx5L in fibroblasts and HeLa cells was obtained using the CRISPR-CAS9 method. For this, pairs of gRNA sequences were designed upstream of the *STX5* initiation codon (crispr.mit.edu, pair 1: ATAAC CTCGG ACTGT TGTGG AGG and ATGAT CCCGC GGAAA CGCTA CGG; pair 2: TAACC TCGGA CTGTT GTGGA GGG and TGATC CCGCG GAAAC GCTAC GGG). The gRNA sequences were cloned in pSpCas9n(BB)-2A-Puro (PX462) V2.0 (gift from Feng Zhang, Addgene no. 62987)<sup>87</sup> and transfected into fibroblasts or HeLa cells by electroporation (Neon Transfection System, Thermofisher, MA). After initial selection with puromycin, the medium was changed for conditioned medium (collected from parental fibroblasts or wildtype HeLa cells at 70% confluency) supplemented 1:1 with fresh medium. Single clones were obtained and screened for knockout of Stx5L by SDS-PAGE and Western blotting.

#### *Immunofluorescence*

Cells were plated on cleaned 12 mm glass coverslips (Electron Microscopy Services, 72230-01) and the following day fixed with 4% paraformaldehyde for 15 minutes at room temperature. Following quenching with 50 mM NH<sub>4</sub>Cl in PBS, cells were permeabilized and blocked in 2% normal donkey serum (Rockland, 017-000-121) and 0.1% saponin (permeabilization buffer) for 30 mins at RT. Primary and secondary antibodies (list of antibodies and dilutions in [Supplementary Table 6](#)) were diluted in permeabilization buffer and incubated for 1 hour at room temperature. Finally, cells were washed with 0.1% Triton X-100 in PBS to remove background staining and mounted with mounting medium containing 0.01% Trolox (6-hydroxy-2,5,7,8-tetramethylchroman-2-carboxylic acid) and 68% glycerol in 200 mM sodium phosphate buffer at pH 7.5 with 0.1 µg/ml DAPI. Coverslips were sealed with nail polish. Cells were imaged on a Leica SP8 SMD confocal laser scanning microscope, equipped

with an HC PL APO CS2 63x/1.20 WATER objective. Colocalization analysis was performed using the *pearsonr* function from the Python package SciPy<sup>88</sup>. Briefly, individual cells were saved to separate .tiff files with ImageJ without any modifications, and then processed in a fully automated and unbiased fashion using the *pearsonr* function.

#### *Lectin stainings*

Cells were plated on cleaned 12 mm glass coverslips for microscopy or 6-wells plates for flow cytometry and after 72 hours culturing fixed with 4% paraformaldehyde. Cells were blocked with Carbo-Free Blocking solution (Vector Laboratories, SP-5040) and incubated with 4 µg/mL biotinylated SNA-I (Vector Laboratories, B-1305) or PNA (Vector Laboratories, B-1075) diluted in Carbo-Free Blocking solution. Cells were then incubated with Streptavidin-Alexa Fluor 647 (ThermoScientific, S32357) before coverslips were mounted as described above. Cells were imaged on a Leica SP8 SMD confocal laser scanning microscope, equipped with an HC PL APO CS2 63x/1.20 WATER objective. For flow cytometry, cells were resuspended in FACS buffer (phosphate buffered saline + 0.5% FBS + 0.01% NaN<sub>3</sub>). Flow cytometry samples were run on a FACSLyric flow cytometer (BD Biosciences) and analyzed with FlowJo X (FlowJo, LLC).

#### *Brefeldin A assay*

Fibroblasts were plated in black clear-bottom 96-wells plates (Greiner, 655090) and cultured until 80% confluent. Cells were either treated with 10 µg/mL Brefeldin A in DMSO (Cayman Chemicals, 11861) or DMSO alone for 6 minutes in a humidified incubator. Washout was performed by washing five times with Leibovitz's L-15 (Gibco 21083027) with 10% FBS, then incubating in Leibovitz's L-15 with 10% FBS at 37°C for the indicated times. After incubation, plates were transferred immediately to ice and cells were fixed with 4% paraformaldehyde, after which the above immunofluorescence protocol was performed. Microscopy images were acquired using a Leica SP8 SMD confocal laser scanning microscope, equipped with an HC PL APO CS2 63x/1.20 WATER objective. HeLa cells were plated on 12 mm coverslips and incubated in the same way with Brefeldin A, but fixed with 100% methanol at -20°C for 15 mins. Imaging of these samples was performed using a Leica DMI6000B epifluorescence microscope equipped with an HC PL APO 63x1.40 OIL objective. Cells were analyzed using Fiji (<http://fiji.sc/>) by first removing noise outliers (bright outliers, radius 2.0 pixels, threshold 50),

then manually selecting cells and measuring the maximum fluorescence intensity in these ROIs. Data were normalized to the mean of the DMSO control of each group.

#### *H-89 assay*

HeLa cells were plated on 12 mm coverslips and incubated the following day for 30 mins with 100  $\mu$ M H-89 (Cayman Chemicals, 10010556) in DMSO or DMSO alone (vehicle) and H-89 was washed out with fresh medium for 5 mins. Cells were fixed with 4% paraformaldehyde for 15 mins at RT and permeabilized with 100% methanol at -20°C for 15 mins prior to immunostaining with ERGIC53 mouse monoclonal antibody (G1/93 or OTI1A8) before epifluorescence imaging as described for the BFA assay. Cells were analyzed using Fiji and the number of ERGIC53-positive spots was quantified with the Spot Counter plugin. Data were normalized to the mean fluorescence of the DMSO control of each group. Data was analyzed with a Mann-Whitney U non-parametric test.

#### *Transmission electron microscopy*

Fibroblasts were grown in 12-wells plates and fixed with 2% glutaraldehyde (Sigma-Aldrich, G5882) in PB (0.1 M phosphate buffer, pH 7.4) for 60 mins at room temperature. Subsequently, cells were washed four times with PB and post-fixed with 1% osmium tetroxide and 1% potassium ferrocyanide in PB for 60 mins at room temperature. Then, cells were again washed four times with PB and four times with water. Cells were incubated overnight in 0.5% uranyl acetate and dehydrated with graded steps of ethanol (30%, 50%, 70%, 96%, 100%) and embedded in Epon resin. 70 nm sections were stained with 2% uranyl acetate solution and lead citrate solution. Stained sections were then examined using a CM12 transmission electron microscope (Phillips).

#### *Live-cell epifluorescence microscopy*

Cells were seeded in four-compartment dishes (Greiner 627870) and transfected as described above (3:1 weight ratio reporter construct:Golgi label). Before imaging, the culture medium was exchanged for Leibovitz's L-15 (Gibco 21083027). Samples were imaged using a DMI6000B (Leica Microsystems) with a heated stage (Pecon) and objective heater. All samples were imaged using an HC PL APO 63x/1.40–0.60 OIL objective. VSVG-ts045-EGFP experiments were performed at 32°C after overnight incubation at 40°C, while all other epifluorescence experiments were performed at 37°C. For RUSH experiments, an equal amount of Leibovitz's L-15 supplemented

with biotin was added to the well immediately before imaging, to reach a final concentration of 40  $\mu$ M biotin. Live cell imaging was started immediately with 15 sec or 30 sec frame rates. Analysis was performed with Fiji, after registration of the image stacks, the increase in fluorescence was measured in the Golgi area by using the thresholded mScarlet-Giantin signal as an image mask.

#### *FRET-FLIM*

All imaging took place in Leibovitz's L-15 supplemented with 10  $\mu$ g/mL cycloheximide (Sigma-Aldrich, C4859) and cells were pulsed with biotin as described above. Imaging was performed on a Leica SP8 SMD system at 37°C, equipped with an HC PL APO CS2 63x/1.20 WATER objective. Fluorophores were excited with a pulsed white light laser, operating at 80 MHz. mCitrine was excited at 514 nm, two separate HyD detectors were used to collect photons, set at 521-565 nm and 613-668 nm respectively. Photons were collected for one minute and lifetime histograms of the donor fluorophore were fitted with monoexponential decay functions convoluted with the microscope instrument response function in Leica LAS X.

#### *Immunoprecipitation*

HeLa cells were lysed 48 hours post-transfection with IP lysis buffer (20 mM Tris-HCl pH 7.6, 137 mM NaCl, 1% IGEPAL, 2 mM EDTA and complete protease inhibitors (Roche 5892791001)). Protein levels were equilibrated and lysates were immunoprecipitated with 1  $\mu$ g anti-GFP-antibody (Rockland 600-401-215) and protein A beads (ThermoFisher, 20333) for 1 hour at 4°C with constant agitation. After three washes with IP lysis buffer, samples were boiled in 5x SDS sample buffer with  $\beta$ -mercaptoethanol and resolved with SDS-PAGE and subsequent immunoblotting.

#### *SDS-PAGE and immunoblotting*

Cells were plated in 12-wells plates in culture medium and lysed the following day with SDS lysis buffer (1% SDS, 10 mM Tris-HCl pH 6.8). Lysates were diluted to equal protein content (30  $\mu$ g per lane) with SDS lysis buffer, separated with SDS-PAGE on 4–20% Mini-PROTEAN TGX Precast Protein Gels (Biorad, 4561094) and subsequently transferred onto 0.45  $\mu$ m PVDF membranes. Small molecular weight proteins (Bet1 and Bet1L) were separated on 16% Schaegger gels<sup>89</sup>.

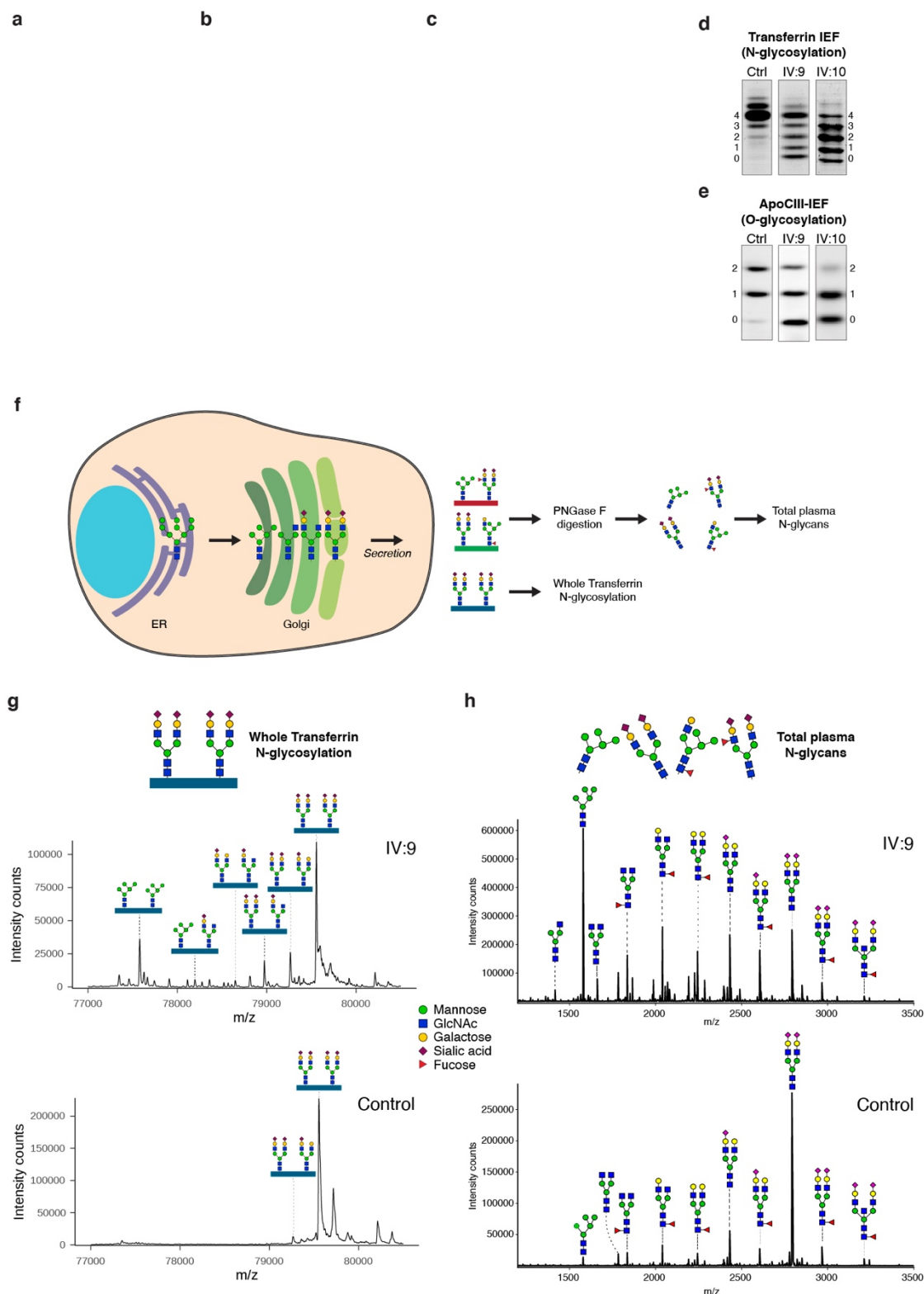
## Quantification and statistical analysis

All mean values represent the average of all cells analyzed. All comparisons between two groups were first checked for similar mean and median values and acceptable ( $< 3x$ ) difference in variance, before statistical analysis with an unpaired two-sided Student's t-test. Relative intensity data was first transformed using the binary logarithm before analysis with an unpaired two-sided Student's t-test. H-89 data was analyzed with a Mann-Whitney U non-parametric test. Stx5 kinetics data were analyzed with a one-way ANOVA, followed by a post-hoc Tukey's honestly significant difference test. Stx5 FLIM data were analyzed with a two-way ANOVA, with the isoform and timepoint as independent variables, followed by a post-hoc Tukey's honestly significant difference test.  $p < 0.05$  was considered significant.  $*p < 0.05$ ,  $**p < 0.01$ ,  $***p < 0.001$ ,  $****p \leq 0.0001$ . All statistical analyses were performed using R statistical software. All numerical data were visualized using R package *ggplot2*<sup>90</sup>, with violins representing the overall distribution of the data and means  $\pm$  95% CI overlaid.

## Data and code availability

Microarray data, exome sequencing data and ImageJ macros for quantification of the RUSH experiments are available upon request. Primary microscopy data was deposited to Zenodo.

## 600 Figures



601 **Figure 1. A novel, lethal, genetic variant suggests a defect in protein glycosylation related to Golgi trafficking.**

602 (a-c) Clinical images of Stx5M55V patients IV:8 (a), IV:9 (b), IV:10 (c).

(d) Glycosylation screening by isoelectric focusing (IEF) of serum transferrin. The accompanying numbers represent the total number of sialic acids in the different proteoforms. Both patients show a reduction in the number of sialic acids. Quantification of bands is shown in [Supplementary Table 2](#).

(e) Glycosylation screening by IEF of serum Apolipoprotein C3 (ApoCIII). ApoCIII has one mucin-type O-linked glycan with one or two sialic acids in controls. Both patients show a reduction in the number of sialic acids. Quantification of bands is shown in [Supplementary Table 2](#).

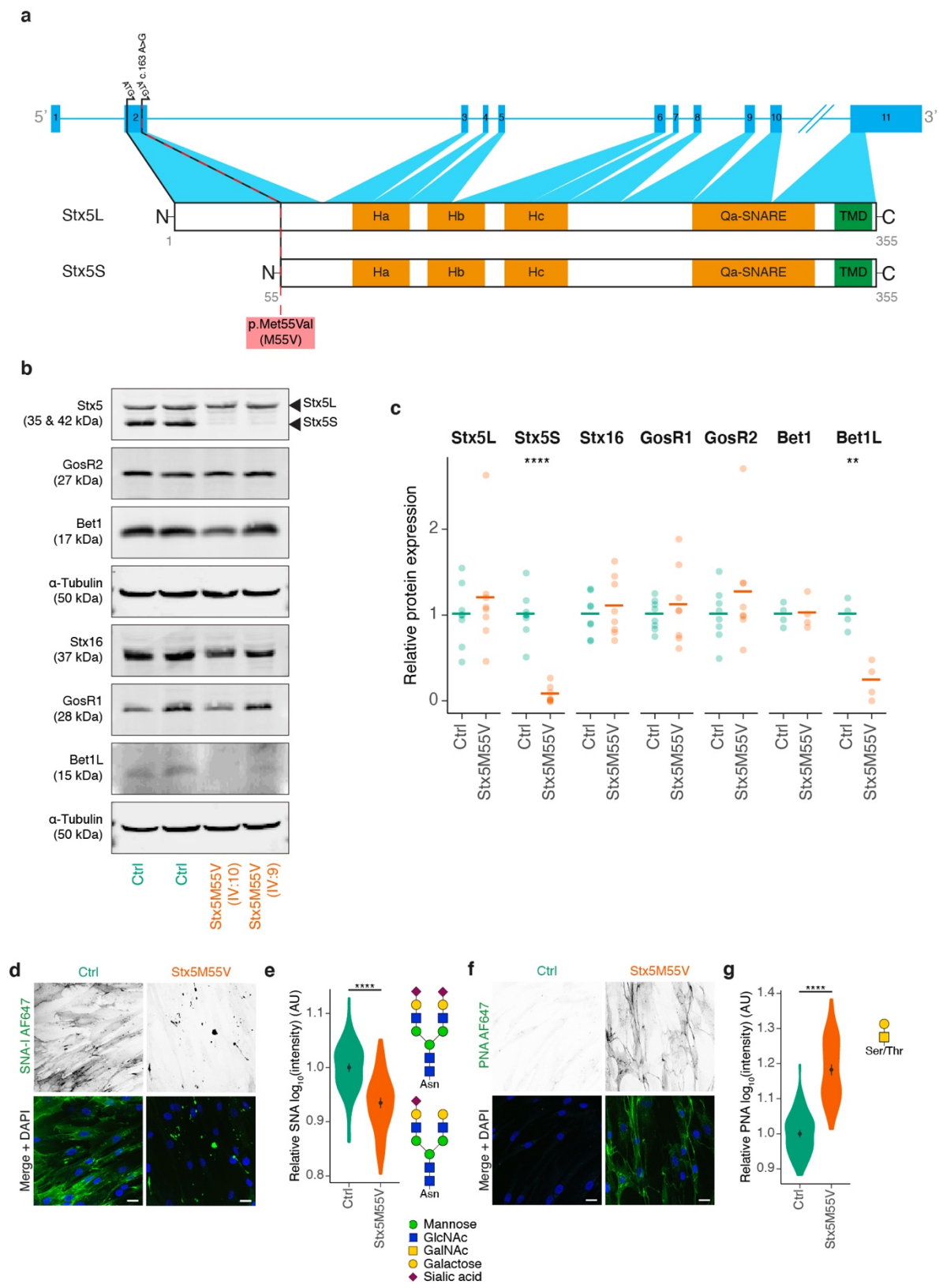
(f) Schematic overview of N-glycosylation intermediates in the Golgi. For mass spectrometry analysis of glycan structures, glycosylated transferrin was enriched from all secreted glycoproteins in human serum and subjected to intact protein mass spectrometry. In parallel, a different serum sample was treated with PNGase F to cleave and analyze N-glycans from all plasma proteins.

(g) Nanochip-C8 QTOF mass spectra of enriched intact serum Transferrin of Stx5M55V patient IV:9 (top spectrum) and healthy control (lower spectrum). Key transferrin glycoforms are shown, indicating a strong increase of high-mannose glycans and glycans lacking sialic acid and galactose. Annotation of all peaks of patients IV:9 and IV:10 is shown in [Supplementary Table 3](#).

(h) MALDI-TOF mass spectra of total plasma N-glycans of Stx5M55V patient IV:9 (top spectrum) and healthy control (lower spectrum). Structural analysis shows a strong increase of high-mannose glycans and glycans lacking sialic acid and galactose. Annotation of all peaks of patients IV:9 and IV:10 is shown in [Supplementary Table 4](#).



622



623

**Figure 2. Primary dermal fibroblasts are an accurate model of the glycosylation defect observed in Stx5M55V patients.**

(a) Schematic representation of the intron-exon structure of *STX5* and the encoded proteoforms resulting from the two starting codons in exon 2. The Stx5M55V genetic variant is indicated by a dashed red line. Orange regions have a secondary helical structure. TMD, transmembrane domain. Ha, Hb, Hc: regulatory Habc-domain.

(b) Representative immunoblot for SNARE proteins of cell lysates of primary human dermal fibroblasts from two unique individual healthy donors (green, Ctrl) or Stx5M55V patients (orange, Stx5M55V).  $\alpha$ -Tubulin, loading control.

(c) Quantification of (b). Protein levels were first normalized to the loading control, then to the average expression of both control lines. Each point represents one cell line from 2 independent experiments.

(d) Fibroblasts of healthy donors (green, Ctrl) or Stx5M55V patients (orange, Stx5M55V) were probed with SNA-I lectin (green in merge). Representative confocal micrographs. Scalebars, 25  $\mu$ m. DAPI in blue.

(e) Quantification of (d). All data were  $\log_{10}$ -transformed and then normalized to the healthy donor. N = 124 (Ctrl) and 111 (Stx5M55V) cells from 2 unique individuals tested twice.

(f-g) Same as panels (d-e), but now for PNA lectin. N = 117 (Ctrl) and 122 (Stx5M55V) cells from 2 unique individuals tested twice.

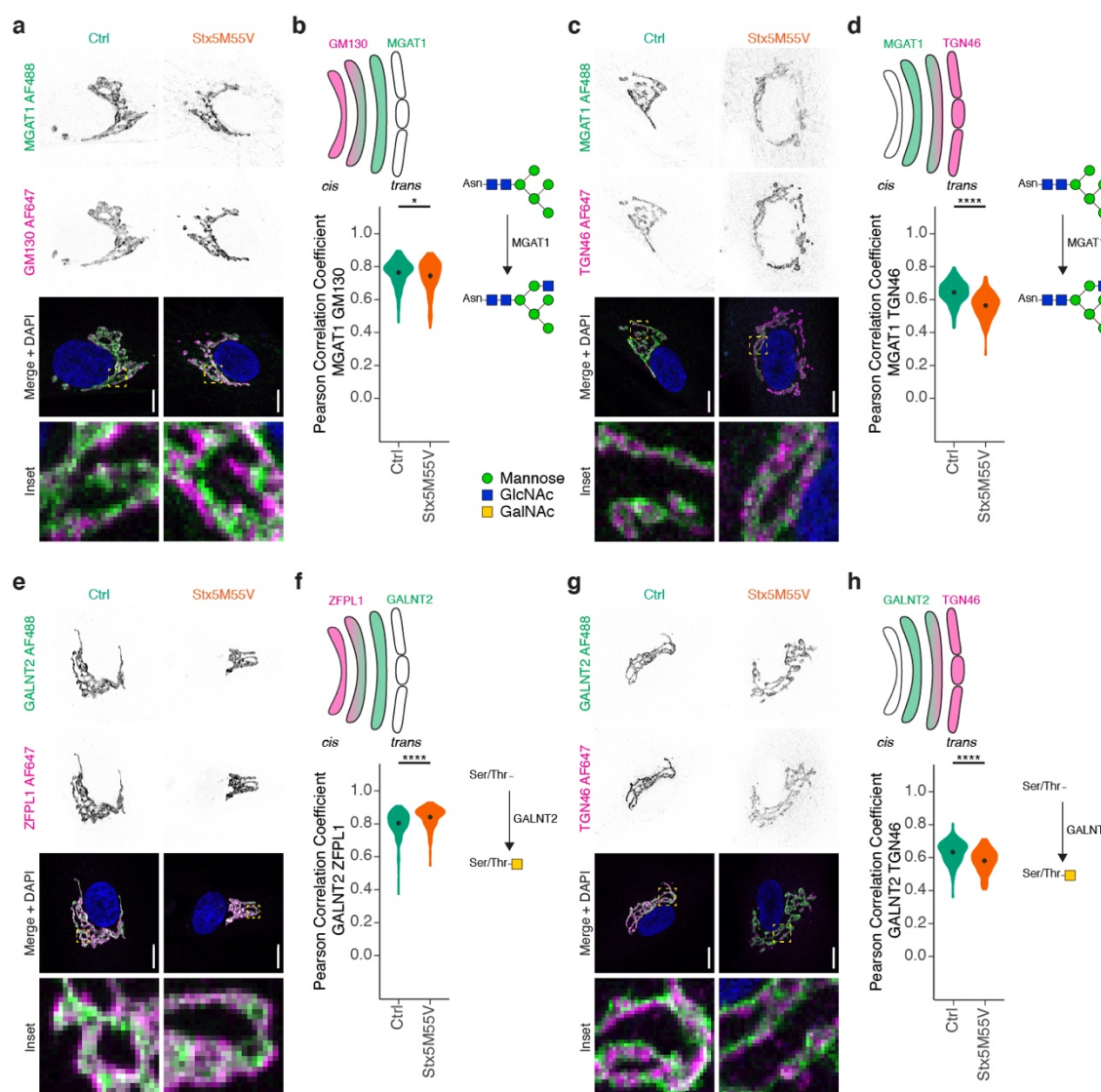


**Figure 3. Glycosylation enzymes mislocalize in Stx5M55V patient fibroblasts.**

- (a) Immunofluorescence microscopy of MGAT1 (green in merge) and GM130 (magenta) in primary dermal fibroblasts of healthy donors (green, Ctrl) or Stx5M55V patients (orange, Stx5M55V). Representative confocal micrographs. Scalebars, 10  $\mu$ m. DAPI in blue. N = 157 (Ctrl) and 126 (Stx5M55V) cells from 2 unique individuals tested twice.
- (b) Pearson's correlations coefficients between MGAT1 and GM130 of panel (a). N = 157 (Ctrl) and 126 (Stx5M55V) from 2 unique individuals tested twice.
- (c-d) Same as panels (a-b), but now for MGAT1 (green) and TGN46 (magenta). N = 157 (Ctrl) and 162 (Stx5M55V) cells from 2 unique individuals tested twice.

650 (e-f) Same as panels (a-b), but now for GALNT2 (green) and ZFPL1 (magenta). N = 240 (Ctrl) and 146 (Stx5M55V)

651 cells from 2 unique individuals tested twice.

652 (g-h) Same as panels (a-b), but now for GALNT2 (green) and TGN46 (magenta). N = 172 (Ctrl) and 152 (Stx5M55V)

653 cells from 2 unique individuals tested twice.

654

655

656

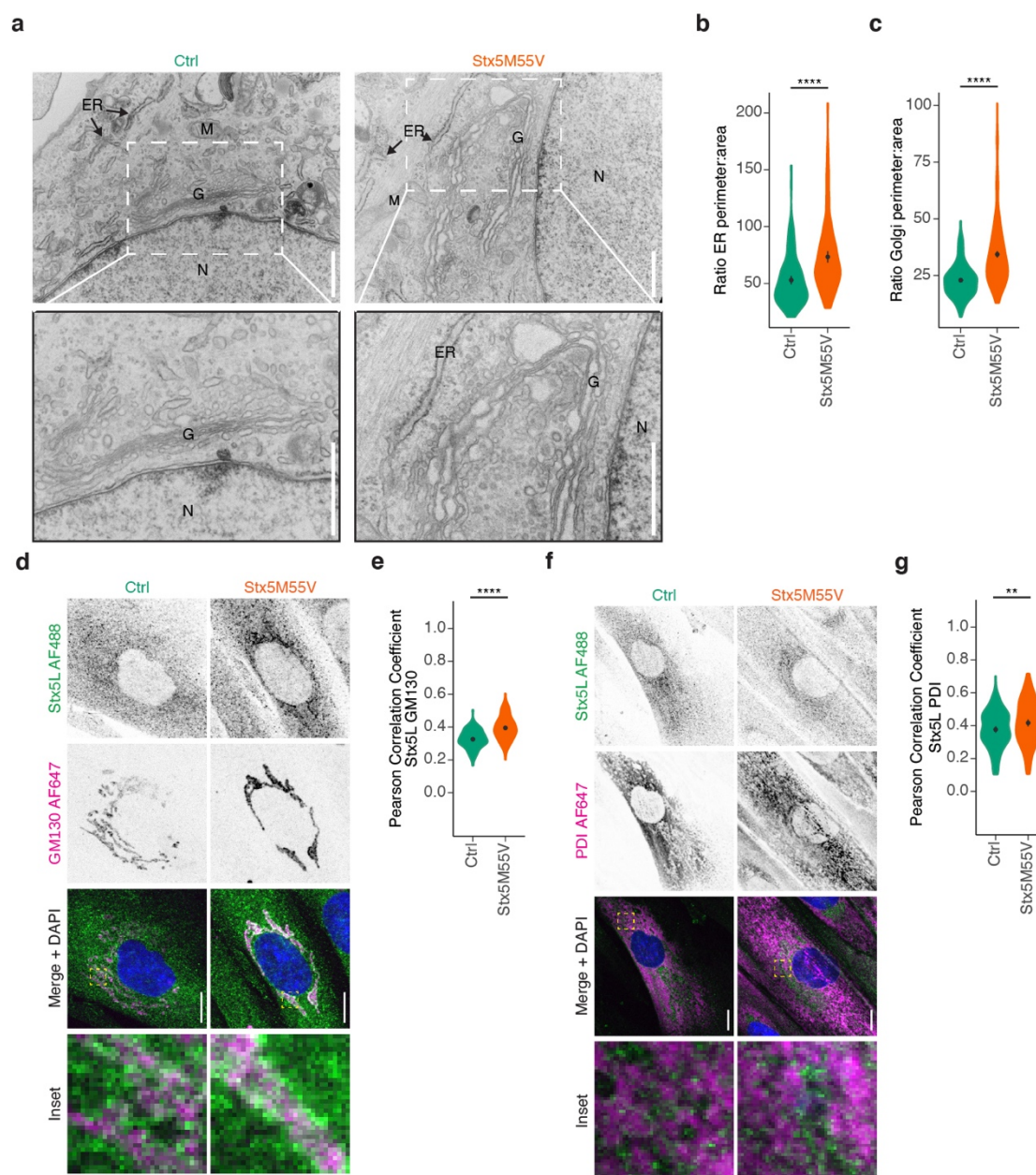


**Figure 4. Loss of Stx5S alters ER and Golgi morphology.**

- (a) Representative transmission electron micrographs from healthy donor fibroblasts (left) or Stx5M55V patient fibroblasts (right). Scalebars, 1  $\mu$ m. N, nucleus; G, Golgi apparatus; ER, endoplasmic reticulum; M, mitochondrion. More electron micrographs in [Supplementary Fig. 9](#).
- (b) ER perimeter and area quantification of panel (a), the ratios of the perimeters over the areas are plotted. N = 144 (both Ctrl and Stx5M55V) ER sections.
- (c) Same as panel (b), but now for Golgi. N = 400 (both Ctrl and Stx5M55V) Golgi sections.

(d) Immunofluorescence microscopy of Stx5L (green in merge) and GM130 (magenta) in primary dermal fibroblasts of healthy donors (green, Ctrl) or Stx5M55V patients (orange, Stx5M55V). Representative confocal micrographs. Scalebars, 10  $\mu$ m. DAPI in blue.

(e) Pearson's correlations coefficients between Stx5L and GM130 of panel (d). N = 102 (Ctrl) and 135 (Stx5M55V) cells from 2 unique individuals tested twice.

(f-g) Same as panels (d-e), but now for Stx5L (green) and TGN46 (magenta). N = 147 (Ctrl) and 156 (Stx5M55V) from 2 unique individuals tested twice.



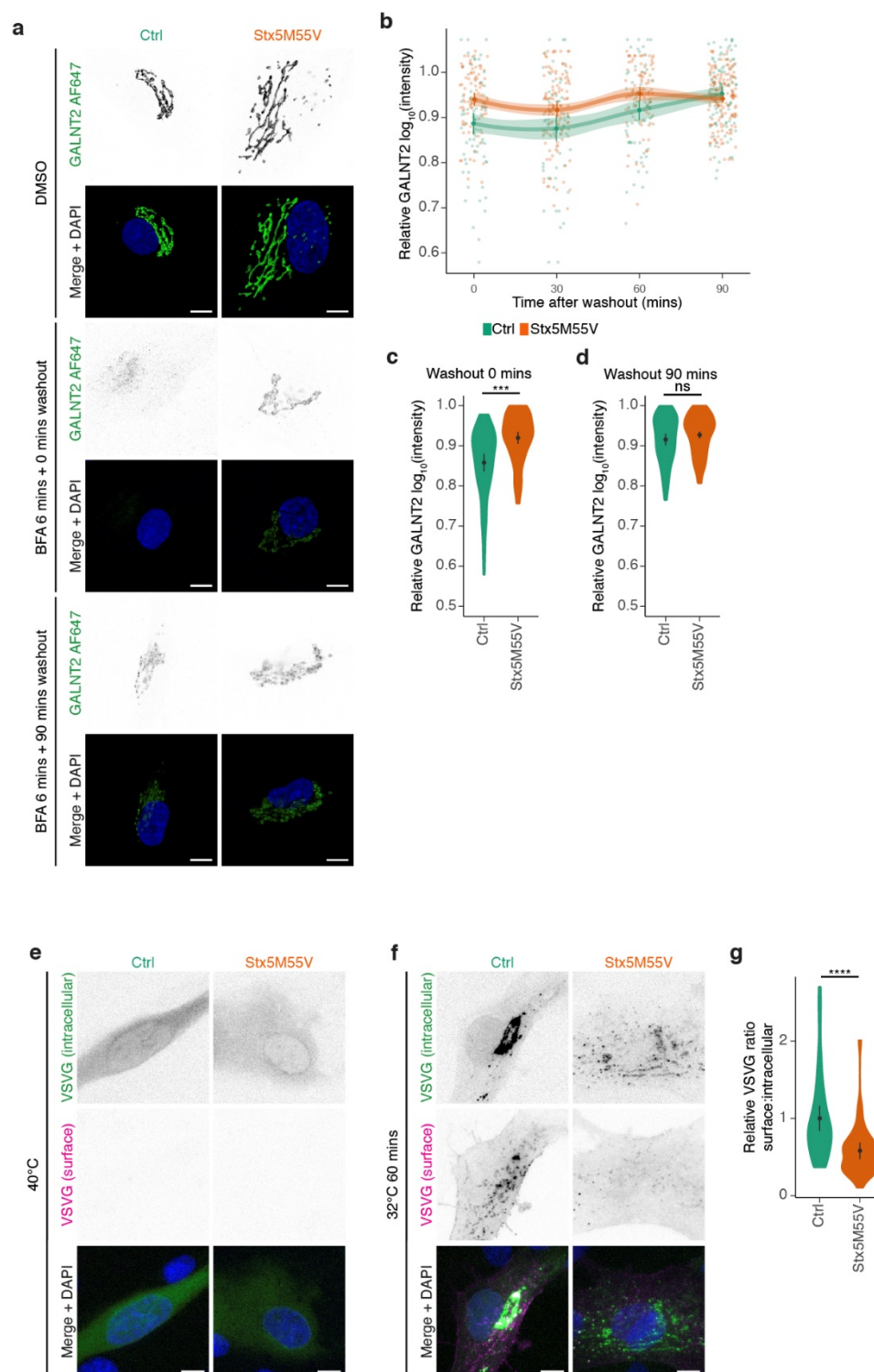


**Figure 5. Loss of Stx5S compromises ER-Golgi trafficking.**

(a) Immunofluorescence microscopy of GALNT2 (green in merge) in primary human dermal fibroblasts of healthy donors (green, Ctrl) or Stx5M55V patients (orange, Stx5M55V) in the absence or presence of

Brefeldin A (BFA) for 6 min and washout for the indicated times. Representative confocal micrographs are shown. Scalebars, 10  $\mu$ m. DAPI in blue.

(b) Timecourse of relative maximum fluorescence intensities of GALNT2 from panel (a). All data were normalized to the DMSO condition (vehicle).

(c) Quantification of the 0 min washout timepoint from panels (a) and (b). N = 76 (Ctrl) and 85 (Stx5M55V) cells from 2 unique individuals tested twice.

(d) Same as (c), but now for the 90 min timepoint. N = 97 (Ctrl) and 152 (Stx5M55V) cells from 2 unique individuals tested twice.

(e) Immunofluorescence microscopy of VSVG-EGFP in primary human dermal fibroblasts of healthy donors (green, Ctrl) or Stx5M55V patients (orange, Stx5M55V) cultured overnight at 40°C. Representative confocal micrographs are shown. Scalebars, 10  $\mu$ m. DAPI in blue.

(f) Same as (e), but now after 60 mins at 32°C.

(g) Quantification of the ratio of surface to intracellular of VSVG after 60 mins at 32°C. N = 45 (Ctrl) and 39 (Stx5M55V) cells from 2 unique individuals tested twice.



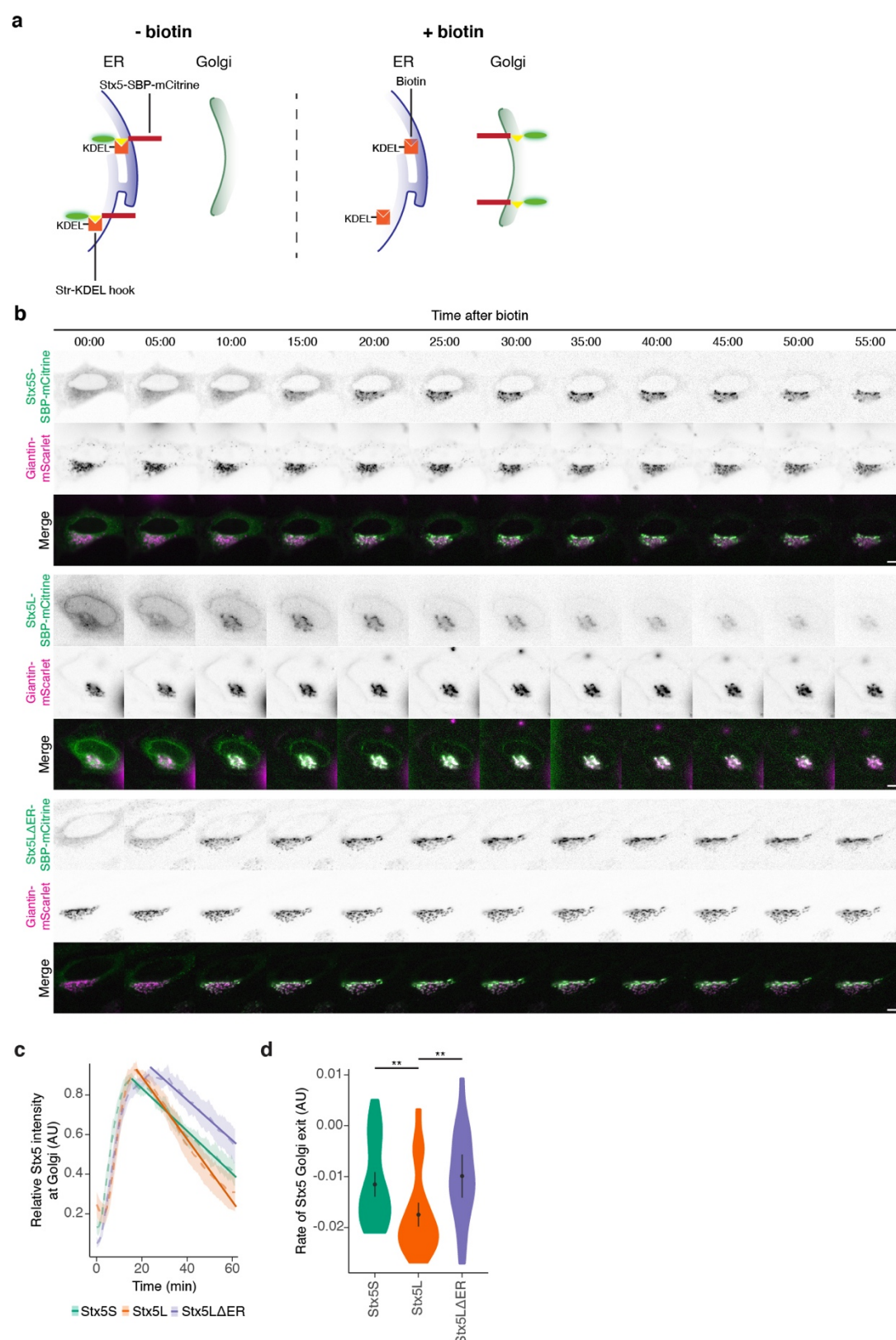


**Figure 6. Faster Golgi exit of Stx5L than Stx5S.**

(a) Schematic overview of the design of Stx5 trafficking experiment, based on the RUSH system. In absence of biotin (left panel), the reporter cargo (Stx5-SBP-mCitrine) is trapped at the ER by the luminal Str-KDEL hook.

694 When biotin is added (right panel), biotin outcompetes the interaction with streptavidin, allowing Stx5-SBP-  
695 mCitrine to traffic freely to its destination compartment. SBP, streptavidin binding protein; Str, streptavidin.  
696 (b) Snapshots of live-cell imaging of Stx5-SBP-mCitrine (green in merge). Magenta: Golgi marker Giantin-  
697 mScarlet. Scale bars, 10  $\mu$ m. See also supplementary movies 5 – 7.

698 (c) Quantification of mCitrine fluorescence at the Golgi of Stx5S-SBP-mCitrine (green), Stx5L-SBP-mCitrine  
699 (orange) and Stx5 $\Delta$ ER-SBP-mCitrine (blue) over time from panel (b). N = 44 (Stx5S), 47 (Stx5L) and 19 (Stx5 $\Delta$ ER)  
700 cells from 4 independent experiments.

701 (d) Quantification of the slopes from panel (c) of the post-Golgi section (~20 mins onwards).  
702

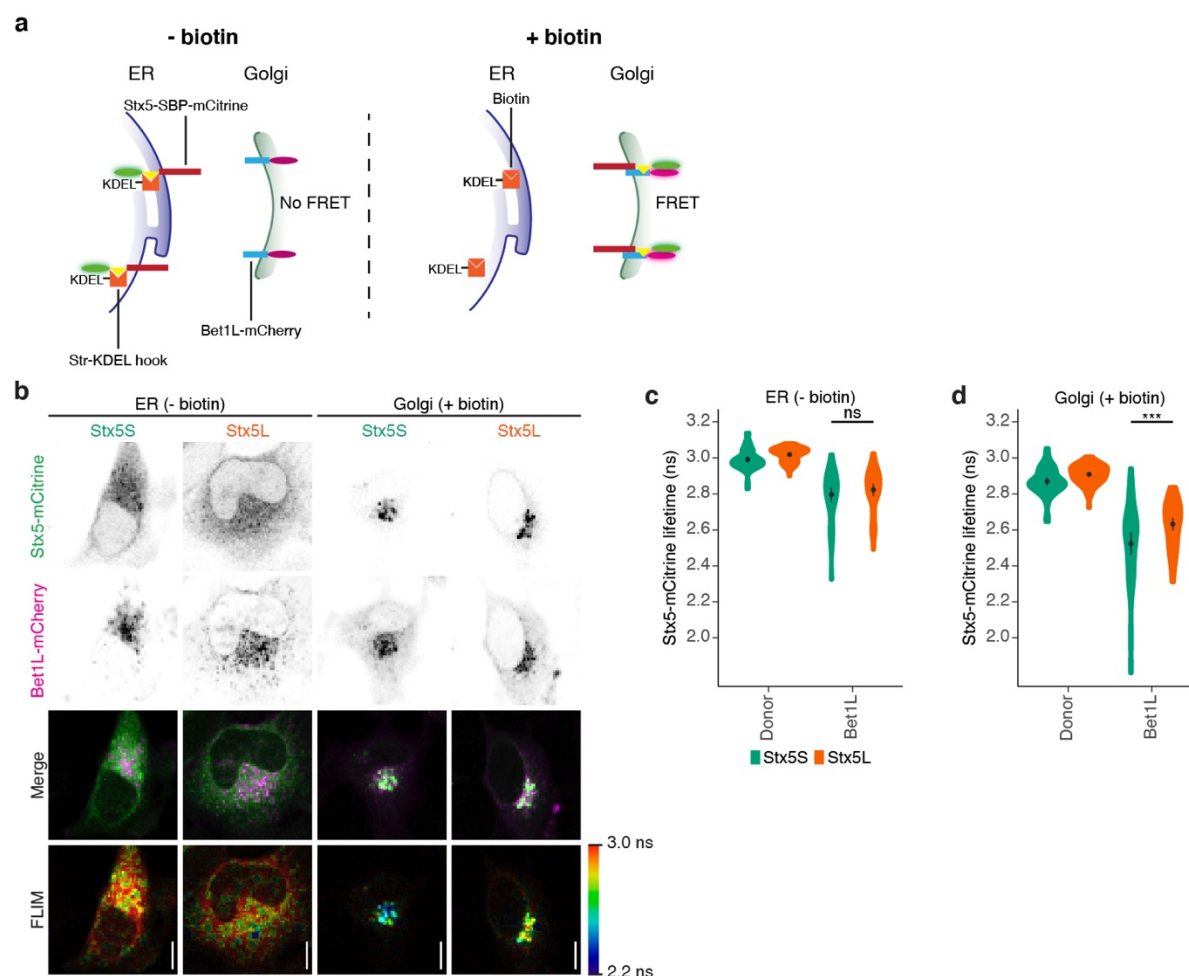


**Figure 7. Stx5S is the dominant Qa-SNARE for intra-Golgi trafficking.**

(a) Schematic overview of experimental design for complex formation of Stx5 isoforms with Bet1L, based on the RUSH system and SNARE complex measurement by FRET-FLIM. In absence of biotin (left panel), the reporter cargo (Stx5-SBP-mCitrine) is trapped at the ER by the luminal Str-KDEL hook, and no FRET with Golgi-localized Bet1L-mCherry occurs. When biotin is added (right panel), biotin outcompetes the interaction with streptavidin, allowing Stx5-SBP-mCitrine to traffic freely to its destination compartment, and SNARE complex formation with Golgi-localized Bet1L-mCherry results in FRET. SBP, streptavidin binding protein; Str, streptavidin; FRET, Förster resonant energy transfer. FLIM, fluorescence lifetime imaging microscopy.

(b) Representative confocal micrographs of HeLa cells co-expressing Stx5-mCitrine (green in merge) and Bet1L-mCherry (magenta) without (ER) or with (Golgi) biotin. Scalebars, 10  $\mu$ m.

(c-d) Stx5-mCitrine lifetimes at the ER (c) and Golgi (d) from panel (b). N = 52 (Stx5S Donor ER), 74 (Stx5L Donor ER), 47 (Stx5S Bet1L ER), 51 (Stx5L Bet1L ER), 50 (Stx5S Donor Golgi), 71 (Stx5L Donor Golgi), 58 (Stx5S Bet1L Golgi) and 58 (Stx5L Bet1L Golgi) cells from 3 independent experiments.

## References

1. Jahn, R. & Scheller, R. H. SNAREs — engines for membrane fusion. *Nature Reviews Molecular Cell Biology* **7**, 631–631 (2006).
2. Banfield, D. K., Lewis, M. J. & Pelham, H. R. B. A SNARE-like protein required for traffic through the Golgi complex. *Nature* **375**, 806–809 (1995).
3. Parlati, F. *et al.* Topological restriction of SNARE-dependent membrane fusion. *Nature* **407**, 194–198 (2000).
4. Parlati, F. *et al.* Distinct SNARE complexes mediating membrane fusion in Golgi transport based on combinatorial specificity. *Proceedings of the National Academy of Sciences of the United States of America* **99**, 5424–9 (2002).
5. Xu, Y., Martin, S., James, D. E. & Hong, W. GS15 Forms a SNARE Complex with Syntaxin 5, GS28, and Ykt6 and Is Implicated in Traffic in the Early Cisternae of the Golgi Apparatus. *MBoC* **13**, 3493–3507 (2002).
6. Bentley, M. *et al.* SNARE status regulates tether recruitment and function in homotypic COPII vesicle fusion. *The Journal of biological chemistry* **281**, 38825–33 (2006).
7. Dascher, C., Matteson, J. & Balch, W. E. Syntaxin 5 regulates endoplasmic reticulum to Golgi transport. *The Journal of biological chemistry* **269**, 29363–6 (1994).
8. Rowe, T., Dascher, C., Bannykh, S., Plutner, H. & Balch, W. E. Role of vesicle-associated syntaxin 5 in the assembly of pre-Golgi intermediates. *Science (New York, N.Y.)* **279**, 696–700 (1998).
9. Xu, D., Joglekar, A. P., Williams, A. L. & Hay, J. C. Subunit structure of a mammalian ER/Golgi SNARE complex. *The Journal of biological chemistry* **275**, 39631–9 (2000).
10. Hay, J. C. *et al.* Localization, Dynamics, and Protein Interactions Reveal Distinct Roles for ER and Golgi SNAREs. *The Journal of Cell Biology* **141**, 1489–1502 (1998).

11. Paek, I. *et al.* ERS-24, a Mammalian v-SNARE Implicated in Vesicle Traffic between the ER and the Golgi. *The Journal of Cell Biology* **137**, 1017–1028 (1997).
12. Zhang, T. *et al.* Ykt6 forms a SNARE complex with syntaxin 5, GS28, and Bet1 and participates in a late stage in endoplasmic reticulum-Golgi transport. *The Journal of biological chemistry* **276**, 27480–7 (2001).
13. Linders, P. T., van der Horst, C., ter Beest, M. & van den Bogaart, G. Stx5-Mediated ER-Golgi Transport in Mammals and Yeast. *Cells* **8**, 780 (2019).
14. Malsam, J. & Söllner, T. H. Organization of SNAREs within the Golgi stack. *Cold Spring Harbor perspectives in biology* **3**, a005249–a005249 (2011).
15. Tai, G. *et al.* Participation of the Syntaxin 5/Ykt6/GS28/GS15 SNARE Complex in Transport from the Early/Recycling Endosome to the Trans-Golgi Network. *MBoC* **15**, 4011–4022 (2004).
16. Dickinson, M. E. *et al.* High-throughput discovery of novel developmental phenotypes. *Nature* **537**, 508–514 (2016).
17. Koscielny, G. *et al.* The International Mouse Phenotyping Consortium Web Portal, a unified point of access for knockout mice and related phenotyping data. *Nucleic Acids Res* **42**, D802–D809 (2014).
18. Hui, N. *et al.* An isoform of the Golgi t-SNARE, syntaxin 5, with an endoplasmic reticulum retrieval signal. *Molecular biology of the cell* **8**, 1777–87 (1997).
19. Gao, G. & Banfield, D. K. Multiple features within the syntaxin Sed5p mediate its Golgi localization. *Traffic* **21**, 274–296 (2020).
20. Dominguez, M. *et al.* gp25L/emp24/p24 protein family members of the cis-Golgi network bind both COP I and II coatomer. *The Journal of cell biology* **140**, 751–65 (1998).

21. Miyazaki, K. *et al.* Contribution of the long form of syntaxin 5 to the organization of the endoplasmic reticulum. *Journal of Cell Science* **125**, 5658 LP – 5666 (2012).
22. Suga, K., Saito, A., Tomiyama, T., Mori, H. & Akagawa, K. The Syntaxin 5 Isoforms Syx5 and Syx5L have Distinct Effects on the Processing of  $\beta$ -amyloid Precursor Protein. *The Journal of Biochemistry* **146**, 905–915 (2009).
23. Avci, D. *et al.* The intramembrane protease SPP impacts morphology of the endoplasmic reticulum by triggering degradation of morphogenic proteins. *J. Biol. Chem.* **294**, 2786–2800 (2019).
24. Hay, J. C., Hirling, H. & Scheller, R. H. Mammalian vesicle trafficking proteins of the endoplasmic reticulum and Golgi apparatus. *J. Biol. Chem.* **271**, 5671–5679 (1996).
25. Shestakova, A., Suvorova, E., Pavliv, O., Khaidakova, G. & Lupashin, V. Interaction of the conserved oligomeric Golgi complex with t-SNARE Syntaxin5a/Sed5 enhances intra-Golgi SNARE complex stability. *The Journal of Cell Biology* **179**, 1179–1192 (2007).
26. Linders, P. T. A., Peters, E., ter Beest, M., Lefeber, D. J. & van den Bogaart, G. Sugary Logistics Gone Wrong: Membrane Trafficking and Congenital Disorders of Glycosylation. *International Journal of Molecular Sciences* **21**, 4654 (2020).
27. Fung, C. W. *et al.* COG5-CDG with a Mild Neurohepatic Presentation. *JIMD Rep* **3**, 67–70 (2012).
28. Paesold-Burda, P. *et al.* Deficiency in COG5 causes a moderate form of congenital disorders of glycosylation. *Hum. Mol. Genet.* **18**, 4350–4356 (2009).
29. Palmigiano, A. *et al.* MALDI-MS profiling of serum O-glycosylation and N-glycosylation in COG5-CDG. *Journal of Mass Spectrometry* **52**, 372–377 (2017).
30. Rymen, D. *et al.* COG5-CDG: expanding the clinical spectrum. *Orphanet J Rare Dis* **7**, 94 (2012).



31. Zhang, T. *et al.* The Mammalian Protein (rbet1) Homologous to Yeast Bet1p Is Primarily Associated with the Pre-Golgi Intermediate Compartment and Is Involved in Vesicular Transport from the Endoplasmic Reticulum to the Golgi Apparatus. *The Journal of Cell Biology* **139**, 1157–1168 (1997).
32. Mallard, F. *et al.* Early/recycling endosomes-to-TGN transport involves two SNARE complexes and a Rab6 isoform. *The Journal of Cell Biology* **156**, 653–664 (2002).
33. Dingjan, I. *et al.* Endosomal and Phagosomal SNAREs. *Physiological Reviews* **98**, 1465–1492 (2018).
34. Pokrovskaya, I. D. *et al.* Conserved oligomeric Golgi complex specifically regulates the maintenance of Golgi glycosylation machinery. *Glycobiology* **21**, 1554–1569 (2011).
35. Chiu, C.-F. *et al.* ZFPL1, a novel ring finger protein required for cis-Golgi integrity and efficient ER-to-Golgi transport. *The EMBO journal* **27**, 934–47 (2008).
36. Gleeson, P. A. *et al.* p230 is associated with vesicles budding from the trans-Golgi network. *Journal of Cell Science* **109**, 2811–2821 (1996).
37. Jaiman, A. & Thattai, M. Golgi compartments enable controlled biomolecular assembly using promiscuous enzymes. *eLife* **9**, e49573 (2020).
38. Reynders, E. *et al.* Golgi function and dysfunction in the first COG4-deficient CDG type II patient. *Hum Mol Genet* **18**, 3244–3256 (2009).
39. Climer, L. K., Pokrovskaya, I. D., Blackburn, J. B. & Lupashin, V. V. Membrane detachment is not essential for COG complex function. *MBoC* **29**, 964–974 (2018).
40. Oka, T. *et al.* Genetic Analysis of the Subunit Organization and Function of the Conserved Oligomeric Golgi (COG) Complex STUDIES OF COG5- AND COG7-DEFICIENT MAMMALIAN CELLS. *J. Biol. Chem.* **280**, 32736–32745 (2005).

41. Glick, B. S. & Nakano, A. Membrane Traffic Within the Golgi Apparatus. *Annual Review of Cell and Developmental Biology* **25**, 113–132 (2009).
42. Galea, G., Bexiga, M. G., Panarella, A., O'Neill, E. D. & Simpson, J. C. A high-content screening microscopy approach to dissect the role of Rab proteins in Golgi-to-ER retrograde trafficking. *J Cell Sci* **128**, 2339–2349 (2015).
43. Lippincott-Schwartz, J., Roberts, T. H. & Hirschberg, K. Secretory Protein Trafficking and Organelle Dynamics in Living Cells. *Annual Review of Cell and Developmental Biology* **16**, 557–589 (2000).
44. Boncompain, G. *et al.* Synchronization of secretory protein traffic in populations of cells. *Nature Methods* **9**, 493–493 (2012).
45. Bindels, D. S. *et al.* mScarlet: a bright monomeric red fluorescent protein for cellular imaging. *Nature Methods* **14**, 53–56 (2017).
46. Verboogen, D. R. J., González Mancha, N., ter Beest, M. & van den Bogaart, G. Fluorescence Lifetime Imaging Microscopy reveals rerouting of SNARE trafficking driving dendritic cell activation. *eLife* **6**, (2017).
47. Griesbeck, O., Baird, G. S., Campbell, R. E., Zacharias, D. A. & Tsien, R. Y. Reducing the Environmental Sensitivity of Yellow Fluorescent Protein MECHANISM AND APPLICATIONS. *J. Biol. Chem.* **276**, 29188–29194 (2001).
48. Casey, J. R., Grinstein, S. & Orlowski, J. Sensors and regulators of intracellular pH. *Nature reviews. Molecular cell biology* **11**, 50–61 (2010).
49. Antonin, W., Holroyd, C., Tikkanen, R., Höning, S. & Jahn, R. The R-SNARE Endobrevin/VAMP-8 Mediates Homotypic Fusion of Early Endosomes and Late Endosomes. *MBoC* **11**, 3289–3298 (2000).



- 834 50. Bajno, L. *et al.* Focal Exocytosis of Vamp3-Containing Vesicles at Sites of Phagosome  
835 Formation. *J Cell Biol* **149**, 697–706 (2000).
- 836 51. Hong, W. SNAREs and traffic. *Biochimica et Biophysica Acta (BBA) - Molecular Cell*  
837 *Research* **1744**, 120–144 (2005).
- 838 52. Manderson, A. P., Kay, J. G., Hammond, L. A., Brown, D. L. & Stow, J. L.  
839 Subcompartments of the macrophage recycling endosome direct the differential  
840 secretion of IL-6 and TNF $\alpha$ . *J Cell Biol* **178**, 57–69 (2007).
- 841 53. Murray, R. Z. A Role for the Phagosome in Cytokine Secretion. *Science* **310**, 1492–1495  
842 (2005).
- 843 54. Amberger, J. S., Bocchini, C. A., Schiettecatte, F., Scott, A. F. & Hamosh, A. OMIM.org:  
844 Online Mendelian Inheritance in Man (OMIM<sup>®</sup>), an online catalog of human genes and  
845 genetic disorders. *Nucleic Acids Res* **43**, D789–D798 (2015).
- 846 55. Pedersen, A. G. & Nielsen, H. Neural network prediction of translation initiation sites in  
847 eukaryotes: perspectives for EST and genome analysis. *Proc Int Conf Intell Syst Mol Biol*  
848 **5**, 226–233 (1997).
- 849 56. Kochetov, A. V. Alternative translation start sites and hidden coding potential of  
850 eukaryotic mRNAs. *BioEssays* **30**, 683–691 (2008).
- 851 57. Kozak, M. Regulation of translation via mRNA structure in prokaryotes and eukaryotes.  
852 *Gene* **361**, 13–37 (2005).
- 853 58. Oka, T., Ungar, D., Hughson, F. M. & Krieger, M. The COG and COPI Complexes Interact  
854 to Control the Abundance of GEARs, a Subset of Golgi Integral Membrane Proteins.  
855 *MBoC* **15**, 2423–2435 (2004).
- 856 59. Ohtsubo, K. & Marth, J. D. Glycosylation in Cellular Mechanisms of Health and Disease.  
857 *Cell* **126**, 855–867 (2006).

60. Freeze, H. H., Chong, J. X., Bamshad, M. J. & Ng, B. G. Solving Glycosylation Disorders: Fundamental Approaches Reveal Complicated Pathways. *The American Journal of Human Genetics* **94**, 161–175 (2014).
61. Fisher, P. & Ungar, D. Bridging the Gap between Glycosylation and Vesicle Traffic. *Front. Cell Dev. Biol.* **4**, (2016).
62. Blackburn, J. B., Kudlyk, T., Pokrovskaya, I. & Lupashin, V. V. More than just sugars: Conserved oligomeric Golgi complex deficiency causes glycosylation-independent cellular defects. *Traffic* **19**, 463–480 (2018).
63. Foulquier, F. *et al.* Conserved oligomeric Golgi complex subunit 1 deficiency reveals a previously uncharacterized congenital disorder of glycosylation type II. *PNAS* **103**, 3764–3769 (2006).
64. Foulquier, F. *et al.* A new inborn error of glycosylation due to a Cog8 deficiency reveals a critical role for the Cog1–Cog8 interaction in COG complex formation. *Hum Mol Genet* **16**, 717–730 (2007).
65. Kranz, C. *et al.* COG8 deficiency causes new congenital disorder of glycosylation type IIh. *Hum Mol Genet* **16**, 731–741 (2007).
66. Miller, V. J. & Ungar, D. Re‘COG’nition at the Golgi. *Traffic* **13**, 891–897 (2012).
67. Morava, E. *et al.* A common mutation in the COG7 gene with a consistent phenotype including microcephaly, adducted thumbs, growth retardation, VSD and episodes of hyperthermia. *Eur J Hum Genet* **15**, 638–645 (2007).
68. Ng, B. G. *et al.* Molecular and clinical characterization of a Moroccan Cog7 deficient patient. *Molecular Genetics and Metabolism* **91**, 201–204 (2007).
69. Wu, X. *et al.* Mutation of the COG complex subunit gene COG7 causes a lethal congenital disorder. *Nat Med* **10**, 518–523 (2004).

70. Huchtagowder, V. *et al.* Loss-of-function mutations in ATP6V0A2 impair vesicular trafficking, tropoelastin secretion and cell survival. *Hum Mol Genet* **18**, 2149–2165 (2009).
71. Jansen, J. C. *et al.* CCDC115 Deficiency Causes a Disorder of Golgi Homeostasis with Abnormal Protein Glycosylation. *The American Journal of Human Genetics* **98**, 310–321 (2016).
72. Jansen, J. C. *et al.* TMEM199 Deficiency Is a Disorder of Golgi Homeostasis Characterized by Elevated Aminotransferases, Alkaline Phosphatase, and Cholesterol and Abnormal Glycosylation. *The American Journal of Human Genetics* **98**, 322–330 (2016).
73. Jansen, E. J. R. *et al.* ATP6AP1 deficiency causes an immunodeficiency with hepatopathy, cognitive impairment and abnormal protein glycosylation. *Nature Communications* **7**, 11600–11600 (2016).
74. Foulquier, F. *et al.* TMEM165 Deficiency Causes a Congenital Disorder of Glycosylation. *The American Journal of Human Genetics* **91**, 15–26 (2012).
75. Ashikov, A. *et al.* Integrating glycomics and genomics uncovers SLC10A7 as essential factor for bone mineralization by regulating post-Golgi protein transport and glycosylation. *Hum Mol Genet* **27**, 3029–3045 (2018).
76. Park, J. H. *et al.* SLC39A8 Deficiency: A Disorder of Manganese Transport and Glycosylation. *The American Journal of Human Genetics* **97**, 894–903 (2015).
77. Witkos, T. M. *et al.* GORAB scaffolds COPI at the trans -Golgi for efficient enzyme recycling and correct protein glycosylation. *Nat Commun* **10**, 1–18 (2019).
78. Zhong, W. Golgi during Development. *Cold Spring Harb Perspect Biol* **3**, (2011).
79. Zhao, H. Membrane Trafficking in Osteoblasts and Osteoclasts: New Avenues for Understanding and Treating Skeletal Diseases. *Traffic* **13**, 1307–1314 (2012).

80. Wagner, T., Dieckmann, M., Jaeger, S., Weggen, S. & Pietrzik, C. U. Stx5 is a novel interactor of VLDL-R to affect its intracellular trafficking and processing. *Experimental Cell Research* **319**, 1956–1972 (2013).
81. Bogaert, A., Fernandez, E. & Gevaert, K. N-Terminal Proteoforms in Human Disease. *Trends in Biochemical Sciences* **45**, 308–320 (2020).
82. Morelle, W. & Michalski, J.-C. Analysis of protein glycosylation by mass spectrometry. *Nature Protocols* **2**, 1585–1602 (2007).
83. van Scherpenzeel, M., Steenbergen, G., Morava, E., Wevers, R. A. & Lefeber, D. J. High-resolution mass spectrometry glycoprofiling of intact transferrin for diagnosis and subtype identification in the congenital disorders of glycosylation. *Translational Research* **166**, 639-649.e1 (2015).
84. Vissers, L. E. L. M. *et al.* A de novo paradigm for mental retardation. *Nature Genetics* **42**, 1109–1112 (2010).
85. Nikopoulos, K. *et al.* Next-Generation Sequencing of a 40 Mb Linkage Interval Reveals TSPAN12 Mutations in Patients with Familial Exudative Vitreoretinopathy. *The American Journal of Human Genetics* **86**, 240–247 (2010).
86. Jolanda, I., de Vries, M., Adema, G. J., Punt, C. J. A. & Figdor, C. G. Phenotypical and Functional Characterization of Clinical-Grade Dendritic Cells. in *Adoptive Immunotherapy: Methods and Protocols* (eds. Ludewig, B. & Hoffmann, M. W.) 113–125 (Humana Press, 2005). doi:10.1385/1-59259-862-5:113.
87. Ran, F. A. *et al.* Genome engineering using the CRISPR-Cas9 system. *Nature Protocols* **8**, 2281–2308 (2013).
88. Virtanen, P. *et al.* SciPy 1.0: fundamental algorithms for scientific computing in Python. *Nature Methods* **17**, 261–272 (2020).

- 930 89. Schgger, H. Tricine–SDS-PAGE. *Nat Protoc* **1**, 16–22 (2006).
- 931 90. Wickham, H. *ggplot2: Elegant Graphics for Data Analysis*. (Springer-Verlag New York,
- 932 2016).
- 933
- 934